The Materials Science *of* Thin Films

Milton Ohring

Stevens Institute of Technology
Department of Materials Science and Engineering
Hoboken, New Jersey

ACADEMIC PRESS, INC.
Harcourt Brace Jovanovich, Publishers

Boston San Diego New York
London Sydney Tokyo Toronto

This book is printed on acid-free paper. ∞

Designed by Elizabeth E. Tustian

ACADEMIC PRESS, INC.
1250 Sixth Avenue, San Diego, CA 92101

United Kingdom Edition published by
ACADEMIC PRESS LIMITED
24–28 Oval Road, London NW1 7DX

Library of Congress Cataloging-in-Publication Data

Ohring, Milton, date.
The materials science of thin films / Milton Ohring.
p. cm.
Includes bibliographical references and index.
ISBN 0-12-524990-X (Alk. paper)
1. Thin films. I. Title.
TA418.9.T45047 1991
620′.44—dc20 91-9664
CIP

Printed in the United States of America
91 92 93 94 9 8 7 6 5 4 3 2 1

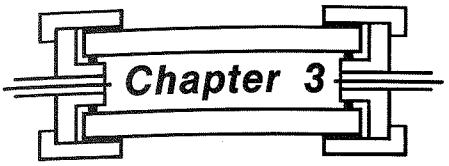

Physical Vapor Deposition

3.1. Introduction

In this chapter we focus on evaporation and sputtering, two of the most important methods for depositing thin films. The objective of these deposition processes is to controllably transfer atoms from a source to a substrate where film formation and growth proceed atomistically. In evaporation, atoms are removed from the source by thermal means, whereas in sputtering they are dislodged from solid target (source) surfaces through impact of gaseous ions. The earliest experimentation in both of these deposition techniques can apparently be traced to the same decade of the nineteenth century. In 1852, Grove (Ref. 1) observed metal deposits sputtered from the cathode of a glow discharge. Five years later Faraday (Ref. 2), experimenting with exploding fuselike metal wires in an inert atmosphere, produced evaporated thin films.

Advances in the development of vacuum-pumping equipment and the fabrication of suitable Joule heating sources, first made from platinum and then tungsten wire, spurred the progress of evaporation technology. Scientific interest in the phenomenon of evaporation and the properties of thin metal films was soon followed by industrial production of optical components such as mirrors, beam splitters, and, later, antireflection coatings. Simultaneously,

sputtering was used as early as 1877 to coat mirrors. Later applications included the coating of flimsy fabrics with Au and the deposition of metal films on wax masters of phonograph records prior to thickening. Up until the late 1960s, evaporation clearly surpassed sputtering as the preferred film deposition technique. Higher deposition rates, better vacuum, and, thus, cleaner environments for film formation and growth, and general applicability to all classes of materials were some of the reasons for the ascendancy of evaporation methods. However, films used for magnetic and microelectronic applications necessitated the use of alloys, with stringent stoichiometry limits, which had to conformally cover and adhere well to substrate surfaces. These demands plus the introduction of radio frequency (RF), bias, and magnetron variants, which extended the capabilities of sputtering, and the availability of high-purity targets and working gases, helped to promote the popularity of sputter deposition. Today the decision of whether to evaporate or sputter films in particular applications is not always obvious and has fostered a lively competition between these methods. In other cases, features of both have been forged into hybrid processes.

Physical vapor deposition (PVD), the term that includes both evaporation and sputtering, and chemical vapor deposition (CVD), together with all of their variant and hybrid processes, are the basic film deposition methods treated in this book. Some factors that distinguish PVD from CVD are:

1. Reliance on solid or molten sources
2. Physical mechanisms (evaporation or collisional impact) by which source atoms enter the gas phase
3. Reduced pressure environment through which the gaseous species are transported
4. General absence of chemical reactions in the gas phase and at the substrate surface (reactive PVD processes are exceptions)

The remainder of the chapter is divided into the following sections:

3.2. The Physics and Chemistry of Evaporation
3.3. Film Thickness Uniformity and Purity
3.4. Evaporation Hardware and Techniques
3.5. Glow Discharges and Plasmas
3.6. Sputtering
3.7. Sputtering Processes
3.8. Hybrid and Modified PVD Processes

Additional excellent reading material on the subject can be found in Refs. 3–6. The book by Chapman is particularly recommended for its entertaining

and very readable presentation of the many aspects relating to phenomena in rarefied gases, glow discharges, and sputtering.

3.2. The Physics and Chemistry of Evaporation

3.2.1. Evaporation Rate

Early attempts to quantitatively interpret evaporation phenomena are connected with the names of Hertz, Knudsen, and, later, Langmuir (Ref. 3). Based on experimentation on the evaporation of mercury, Hertz, in 1882, observed that evaporation rates were:

1. Not limited by insufficient heat supplied to the surface of the molten evaporant
2. Proportional to the difference between the equilibrium pressure P_e of Hg at the given temperature and the hydrostatic pressure P_h acting on the evaporant.

Hertz concluded that a liquid has a specific ability to evaporate at a given temperature. Furthermore, the maximum evaporation rate is attained when the number of vapor molecules emitted corresponds to that required to exert the equilibrium vapor pressure while none return. These ideas led to the basic equation for the rate of evaporation from both liquid and solid surfaces, namely,

$$\Phi_e = \frac{\alpha_e N_A (P_e - P_h)}{\sqrt{2\pi MRT}}, \tag{3-1}$$

where Φ_e is the evaporation flux in number of atoms (or molecules) per unit area per unit time, and α_e is the coefficient of evaporation, which has a value between 0 and 1. When $\alpha_e = 1$ and P_h is zero, the maximum evaporation rate is realized. By analogy with Eq. 2-9, an expression for the maximum value of Φ_e is

$$\Phi_e = 3.513 \times 10^{22} \frac{P_e}{\sqrt{MT}} \text{ molecules/cm}^2\text{-sec}. \tag{3-2}$$

When P_e is expressed in torr, a useful variant of this formula is

$$\Gamma_e = 5.834 \times 10^{-2} \sqrt{M/T}\, P_e \text{ g/cm}^2\text{-sec}, \tag{3-3}$$

where Γ_e is the mass evaporation rate. At a pressure of 10^{-2} torr, a typical value of Φ_e for many elements is approximately 10^{-4} g/cm^2-sec of evaporant area. The key variable influencing evaporation rates is the temperature, which has a profound effect on the equilibrium vapor pressure.

3.2.2. Vapor Pressure of the Elements

A convenient starting point for expressing the connection between temperature and vapor pressure is the Clausius–Clapeyron equation, which for both solid–vapor and liquid–vapor equilibria can be written as

$$\frac{dP}{dT} = \frac{\Delta H(T)}{T\Delta V}. \tag{3-4}$$

The changes in enthalphy, $\Delta H(T)$, and volume, ΔV, refer to differences between the vapor (v) and the particular condensed phase (c) from which it originates, and T is the transformation temperature in question. Since $\Delta V = V_v - V_c$, and the volume of vapor normally considerably exceeds that of the condensed solid or liquid phase, $\Delta V = V_v$. If the gas is assumed to be perfect, $V_v \approx RT/P$, and Eq. 3-4 may be rewritten as

$$\frac{dP}{dT} = \frac{P\Delta H(T)}{RT^2}. \tag{3-5}$$

As a first approximation, $\Delta H(T) = \Delta \mathrm{He}$, the molar heat of evaporation (a constant), in which case simple integration yields

$$\ln P \approx -\frac{\Delta \mathrm{He}}{RT} + I, \tag{3-6}$$

where I is a constant of integration. Through substitution of the latent heat of vaporization for ΔHe, the boiling point for T, and 1 atm for P, I can be evaluated for the liquid–vapor transformation. For practical purposes, Eq. 3-6 adequately describes the temperature dependence of the vapor pressure in many materials. It is rigorously applicable only over a small temperature range, however. To extend the range of validity, we must account for the temperature dependence of $\Delta H(T)$. For example, careful evaluation of thermodynamic data reveals that the vapor pressure of liquid Al is given by (Ref. 3)

$$\log P_{(\mathrm{torr})} = 15{,}993/T + 12.409 - 0.999 \log T - 3.52 \times 10^{-6} T. \tag{3-7}$$

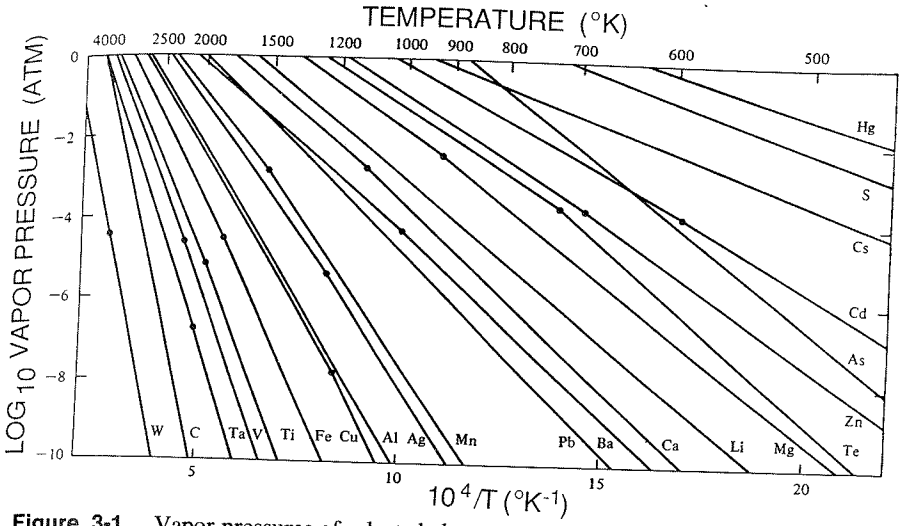

Figure 3-1. Vapor pressures of selected elements. Dots correspond to melting points. (From Ref. 7).

The Arrhenius character of log P vs. $1/T$ is essentially preserved, since the last two terms on the right-hand side are small corrections.

Vapor-pressure data for many other metals have been similarly obtained and conveniently represented as a function of temperature in Fig. 3-1. Similarly, vapor-pressure data for elements important in the deposition of semiconductor films are presented in Fig. 3-2. Much of the data represent direct measurements of the vapor pressures. Other values are inferred indirectly from thermodynamic relationships and identities using a limited amount of experimental data. Thus the vapor pressures of refractory metals such as W and Mo can be unerringly extrapolated to lower temperatures, even though it may be impossible to measure them directly.

Two modes of evaporation can be distinguished in practice, depending on whether the vapor effectively emanates from a liquid or solid source. As a rule of thumb, a melt will be required if the element in question does not achieve a vapor pressure greater than 10^{-3} torr at its melting point. Most metals fall into this category, and effective film deposition is attained only when the source is heated into the liquid phase. On the other hand, elements such as Cr, Ti, Mo, Fe, and Si reach sufficiently high vapor pressures below the melting point and, therefore, sublime. For example, Cr can be effectively deposited at high rates from a solid metal source because it attains vapor pressures of 10^{-2} torr some 500 °C below the melting point. The operation of the Ti sublimation pump mentioned in Chapter 2 is, in fact, based on the sublimation from heated Ti

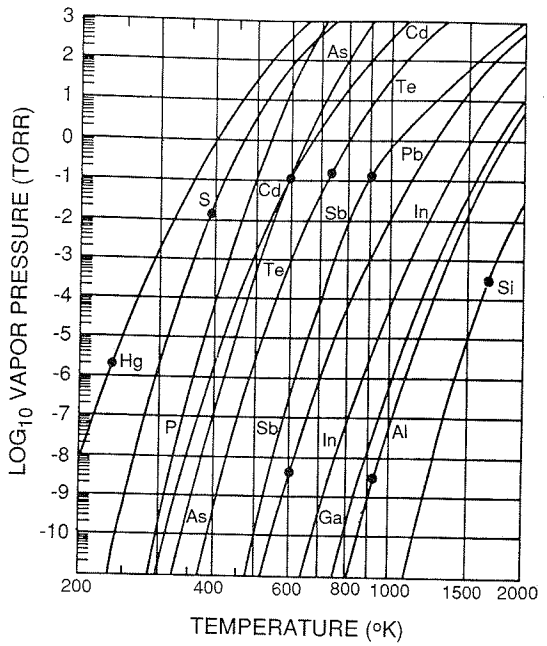

Figure 3-2. Vapor pressures of elements employed in semiconductor materials. Dots correspond to melting points. (Adapted from Ref. 8).

filaments. A third example is carbon, which is used to prepare replicas of the surface topography of materials for subsequent examination in the electron microscope. The carbon is sublimed from an arc struck between graphite electrodes.

3.2.3. Evaporation of Compounds

While metals essentially evaporate as atoms and occasionally as clusters of atoms, the same is not true of compounds. Very few inorganic compounds evaporate without molecular change, and, therefore, the vapor composition is usually different from that of the original solid or liquid source. A consequence of this is that the stoichiometry of the film deposit will generally differ from that of the source. Mass spectroscopic studies of the vapor phase have shown that the processes of molecular association as well as dissociation frequently occur. A broad range of evaporation phenomena in compounds occurs, and these are categorized briefly in Table 3-1.

Table 3-1. Evaporation of Compounds

Reaction Type	Chemical Reaction	Examples	Comments
Evaporation without dissociation	$MX(s \text{ or } l) \rightarrow MX(g)$	SiO, B_2O_3 GeO, SnO, AlN CaF_2, MgF_2	Compound stoichiometry maintained in deposit
Decomposition	$MX(s) \rightarrow M(s) + (1/2)X_2(g)$	Ag_2S, Ag_2Se	Separate sources are required to deposit these compounds
	$MX(s) \rightarrow M(l) + (1/n)X_n(g)$	III-V semiconductors	
Evaporation with dissociation			
a. Chalcogenides X = S, Se, Te	$MX(s) \rightarrow M(g) + (1/2)X_2(g)$	CdS, CdSe CdTe	Deposits are metal-rich; separate sources are required to deposit these compounds
b. Oxides	$MO_2(s) \rightarrow MO(g) + (1/2)O_2(g)$	SiO_2, GeO_2 TiO_2, SnO_2 ZrO_2	Metal-rich discolored deposits; dioxides are best deposited in O_2 partial pressure (reactive evaporation)

Note M = metal, X = nonmetal.
Adapted from Ref. 3.

3.2.4. Evaporation of Alloys

Evaporated metal alloy films are widely utilized for a variety of electronic, magnetic, and optical applications as well as for decorative coating purposes. Important examples of such alloys that have been directly evaporated include Al–Cu, Permalloy (Fe–Ni), nichrome (Ni–Cr), and Co–Cr. Atoms in metals of such alloys are generally less tightly bound than atoms in the inorganic compounds discussed previously. The constituents of the alloys, therefore, evaporate nearly independently of each other and enter the vapor phase as single atoms in a manner paralleling the behavior of pure metals. Metallic melts are solutions and as such are governed by well-known thermodynamic

laws. When the interaction energy between A and B atoms of a binary AB alloy melt are the same as between A–A and B–B atom pairs, then no preference is shown for atomic partners. Such is the environment in an ideal solution. Raoult's law, which holds under these conditions, states that the vapor pressure of component B in solution is reduced relative to the vapor pressure of pure B ($P_B(0)$) in proportion to its mole fraction X_B. Therefore,

$$P_B = X_B P_B(0). \tag{3-8}$$

Metallic solutions usually are not ideal, however. This means that either more or less B will evaporate relative to the ideal solution case, depending on whether the deviation from ideality is positive or negative, respectively. A positive deviation occurs because B atoms are physically bound less tightly to the solution, facilitating their tendency to escape or evaporate. In real solutions

$$P_B = a_B P_B(0), \tag{3-9}$$

where a_B is the effective thermodynamic concentration of B known as the activity. The activity is, in turn, related to X_B through an activity coefficient γ_B; i.e.,

$$a_B = \gamma_B X_B. \tag{3-10}$$

By combination of Eqs. 3-2, 3-9, and 3-10, the ratio of the fluxes of A and B atoms in the vapor stream above the melt is given by

$$\frac{\Phi_A}{\Phi_B} = \frac{\gamma_A X_A P_A(0)}{\gamma_B X_B P_B(0)} \sqrt{\frac{M_B}{M_A}}. \tag{3-11}$$

Practical application of this equation is difficult because the melt composition changes as evaporation proceeds. Therefore, the activity coefficients, which can sometimes be located in the metallurgical literature, but just as frequently not, also change with time. As an example of the use of Eq. 3-11, consider the problem of estimating the approximate Al–Cu melt composition required to evaporate films containing 2 wt% Cu from a single crucible heated to 1350 K. Substituting gives

$$\frac{\Phi_{Al}}{\Phi_{Cu}} = \frac{98/M_{Al}}{2/M_{Cu}}, \qquad \frac{P_{Al}(0)}{P_{Cu}(0)} = \frac{10^{-3}}{2 \times 10^{-4}} \qquad \text{and assuming } \gamma_{Cu} = \gamma_{Al},$$

$$\frac{X_{Al}}{X_{Cu}} = \frac{98}{2} \frac{2 \times 10^{-4}}{10^{-3}} \sqrt{\frac{63.7}{27.0}} = 15.$$

This suggests that the original melt composition should be enriched to 13.6 wt% Cu in order to compensate for the preferential vaporization of Al. It is, therefore, feasible to evaporate such alloys from one heated source. If the alloy

melt is of large volume, fractionation-induced melt composition changes are minimal. A practical way to cope with severe fractionation is to evaporate from dual sources maintained at different temperatures.

3.3. Film Thickness Uniformity and Purity

3.3.1. Deposition Geometry

In this section aspects of the deposition geometry, including the characteristics of evaporation sources, and the orientation and placement of substrates are discussed. The source–substrate geometry, in turn, influences the ultimate film uniformity, a concern of paramount importance, which will be treated subsequently. Evaporation from a point source is the simplest of situations to model. Evaporant particles are imagined to emerge from an infinitesimally small region (dA_e) of a sphere of surface area A_e with a uniform mass evaporation rate as shown in Fig. 3-3a. The total evaporated mass $\overline{M}_e$ is then given by the double integral

$$\overline{M}_e = \int_0^t \int_{A_e} \Gamma_e \, dA_e \, dt. \tag{3-12}$$

Of this amount, mass $d\overline{M}_s$ falls on the substrate of area dA_s. Since the projected area dA_s on the surface of the sphere is dA_c, with $dA_c = dA_s \cos\theta$, the proportionality $d\overline{M}_s : \overline{M}_e = dA_c : 4\pi r^2$ holds. Finally,

$$\frac{d\overline{M}_s}{dA_s} = \frac{\overline{M}_e \cos\theta}{4\pi r^2} \tag{3-13}$$

is obtained. On a per unit time basis we speak of deposition rate $\dot{R}$ (atoms/cm^2-sec), a related quantity referred to later in the book. The deposi-

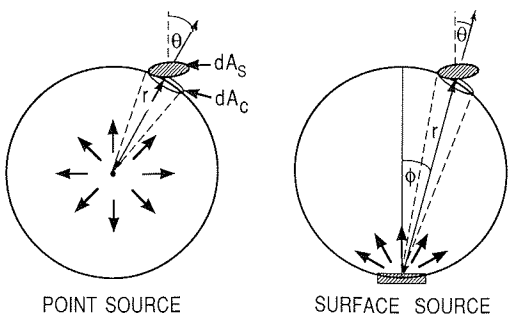

Figure 3-3. Evaporation from (a) point source, (b) surface source.

tion varies with the geometric orientation of the substrate and with the inverse square of the source–substrate distance. Substrates placed tangent to the surface of the receiving sphere would be coated uniformly, since $\cos\theta = 1$.

An evaporation source employed in the pioneering research by Knudsen made use of an isothermal enclosure with a very small opening through which the evaporant atoms or molecules effused. These effusion or Knudsen cells are frequently employed in molecular-beam epitaxy deposition systems, where precise control of evaporation variables is required. Kinetic theory predicts that the molecular flow of the vapor through the opening is directed according to a cosine distribution law, and this has been verified experimentally. The mass deposited per unit area is given by

$$\frac{d\overline{M}_s}{dA_s} = \frac{\overline{M}_e \cos\phi\cos\theta}{\pi r^2} \tag{3-14}$$

and now depends on two angles (emission and incidence) that are defined in Fig. 3-3b. Evaporation from a small area or surface source is also modeled by Eq. 3-14. Boat filaments and wide crucibles containing a pool of molten material to be evaporated approximate surface sources in practice.

From careful measurements of the angular distribution of film thickness, it has been found that, rather than a $\cos\phi$ dependence, a $\cos^n\phi$ evaporation law is more realistic. As shown in Fig. 3-4, n is a number that determines the geometry of the lobe-shaped vapor cloud and the angular distribution of evaporant flux from a source. When n is large, the vapor flux is highly directed. Physically n is related to the evaporation crucible geometry and scales directly with the ratio of the melt depth (below top of crucible) to the

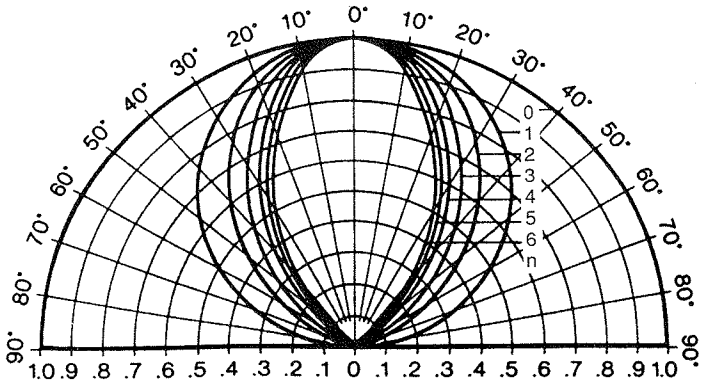

Figure 3-4. Calculated lobe-shaped vapor clouds with various cosine exponents. (From Ref. 9).

melt surface area. Deep narrow crucibles with large n have been employed to confine evaporated radioactive materials to a narrow angular spread in order to minimize chamber contamination. The corresponding deposition equation is (Ref. 9)

$$\frac{d\overline{M}_s}{dA_s} = \frac{\overline{M}_e(n+1)\cos^n\phi\cos\theta}{2\pi r^2} \qquad (n \geq 0). \tag{3-15}$$

As the source becomes increasingly directional, the surface area effectively exposed to evaporant shrinks (i.e., $2\pi r^2$, πr^2, and $2\pi r^2/(n+1)$ for point, $\cos\phi$, and $\cos^n\phi$ sources, respectively).

3.3.2. Film Thickness Uniformity

While maintaining thin-film thickness uniformity is always desirable, but not necessarily required, it is absolutely essential for microelectronic and many optical coating applications. For example, thin-film, narrow-band optical interference filters require a thickness uniformity of $\pm 1\%$. This poses a problem, particularly if there are many components to be coated or the surfaces involved are large or curved. Utilizing formulas developed in the previous section, we can calculate the thickness distribution for a variety of important source–substrate geometries. Consider evaporation from the point and small surface source onto a *parallel* plane-receiving substrate surface as indicated in the insert of Fig. 3-5. The film thickness d is given by $d\overline{M}_s/\rho\, dA_s$, where ρ is the density of the deposit. For the point source

$$d = \frac{\overline{M}_e\cos\theta}{4\pi\rho r^2} = \frac{\overline{M}_e h}{4\pi\rho r^3} = \frac{\overline{M}_e h}{4\pi\rho\left(h^2+l^2\right)^{3/2}}. \tag{3-16}$$

The thickest deposit (d_0) occurs at $l = 0$, in which case $d_0 = \overline{M}_e/4\pi\rho h^2$, and, thus,

$$\frac{d}{d_0} = \frac{1}{\left\{1+(l/h)^2\right\}^{3/2}}. \tag{3-17}$$

Similarly, for the surface source

$$d = \frac{\overline{M}_e\cos\theta\cos\phi}{\pi\rho r^2} = \frac{\overline{M}_e}{\pi\rho r^2}\frac{h}{r}\frac{h}{r} = \frac{\overline{M}_e h^2}{\pi\rho\left(h^2+l^2\right)^2}, \tag{3-18}$$

since $\cos\theta = \cos\phi = h/r$. When normalized to the thickest dimensions, or $d_0 = \overline{M}_e/\pi\rho h^2$,

$$\frac{d}{d_0} = \frac{1}{\left\{1+(l/h)^2\right\}^2}. \tag{3-19}$$

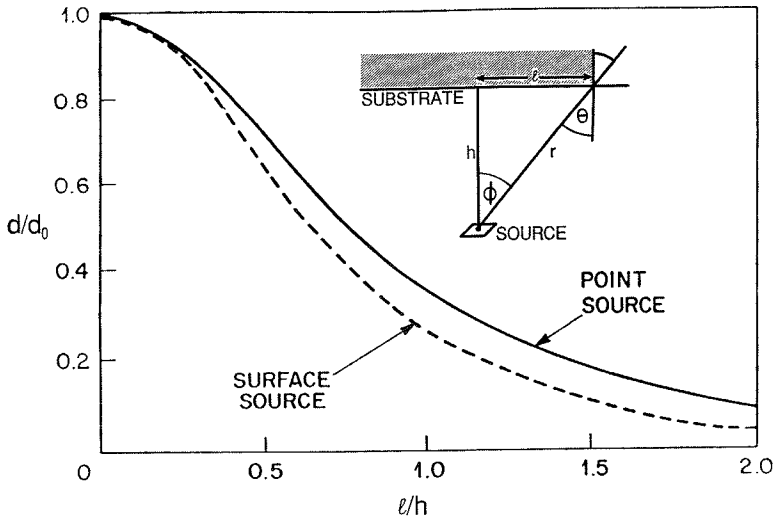

Figure 3-5. Film thickness uniformity for point and surface sources. (Insert) Geometry of evaporation onto parallel plane substrate.

A comparison of Eqs. 3-17 and 3-19 is made in Fig. 3-5, where it is apparent that less thickness uniformity can be expected with the surface source.

A couple of practical examples (Ref. 10) will demonstrate how these film thickness distributions are used in designing source–substrate geometries for coating applications. In the first example suppose it is desired to coat a 150-cm-wide strip utilizing two evaporation sources oriented as shown in the insert of Fig. 3-6. If a thickness tolerance of $\pm 10\%$ is required, what should the distance between sources be and how far should they be located from the substrate? A superposition of solutions for two individual surface sources (Eq. 3-19) gives the thickness variation shown graphically in Fig. 3-6 as a function of the relative distance r from the center line for various values of the source spacing D. All pertinent variables are in terms of dimensionless ratios r/h_v and D/h_v. The desired tolerance requires that d/d_0 stay between 0.9 and 1.1, and this can be achieved with $D/h_v = 0.6$ yielding a maximum value of $r/h_v = 0.87$. Since $r = 150/2 = 75$ cm, $h_v = 75/0.87 = 86.2$ cm. The required distance between sources is therefore $D = 2 \times 0.6 \times 86.2 = 103.4$ cm. There are other solutions, of course, but we are seeking the *minimum* value of h_v. It is obvious that the uniformity tolerance can always be realized by extending the source–substrate distance, but this wastes evaporant.

As a second example, consider a composite optical coating where a $\pm 1\%$ film thickness variation is required in each layer. The substrate is rotated to even out source distribution anomalies and minimize preferential film growth

that can adversely affect coating durability and optical properties. Since multiple films of different composition will be sequentially deposited, the necessary fixturing requires that the sources be offset from the axis of rotation by a distance $R = 20$ cm. How high above the source should a 25-cm-diameter substrate be rotated to maintain the desired film tolerance? The film thickness distribution in this case is a complex function of the three-dimensional geometry, which, fortunately, has been graphed in Fig. 3-7. Reference to this figure indicates that the curve $h_v/R = 1.33$ in conjunction with $r/R = 0.6$ will generate a thickness deviation ranging from about -0.6 to $+0.5\%$. On this basis, the required distance is $h_v = 1.33 \times 20 = 26.6$ cm.

A clever way to achieve thickness uniformity, however, is to locate both the surface evaporant source and the substrates on the surface of a sphere as shown in Fig. 3-8. In this case, $\cos\theta = \cos\phi = r/2r_0$, and Eq. 3-14 becomes

$$\frac{d\overline{M}_s}{dA_s} = \frac{\overline{M}_e}{\pi r^2}\frac{r}{2r_0}\frac{r}{2r_0} = \frac{\overline{M}_e}{4\pi r_0^2}. \tag{3-20}$$

The resultant deposit thickness is a constant clearly independent of angle. Use is made of this principle in the planetary substrate fixtures that hold silicon wafers to be coated with metal (metalized) by evaporation. To further promote uniform coverage, the planetary fixture is rotated during deposition. Physi-

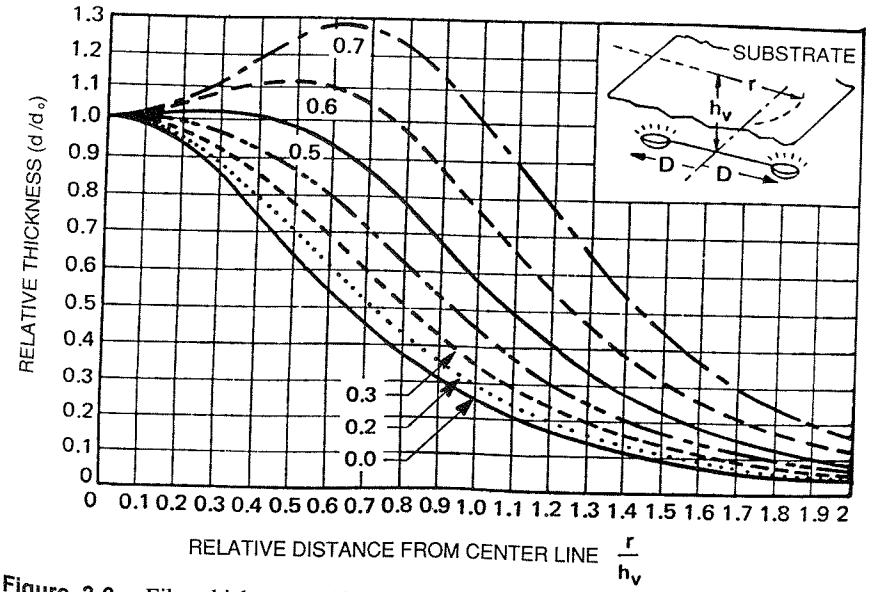

Figure 3-6. Film thickness uniformity across a strip employing two evaporation sources for various values of D/h_v. (From Ref. 10).

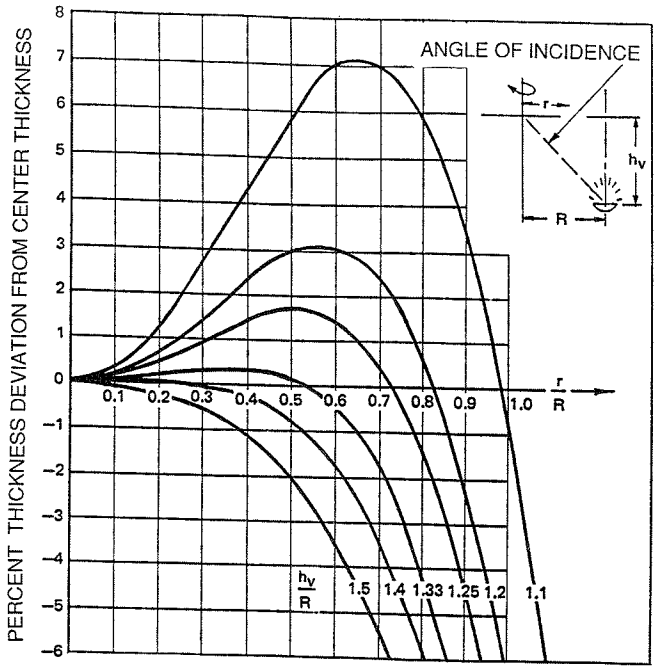

Figure 3-7. Calculated film thickness variation across the radius of a rotating disk. (From Ref. 10).

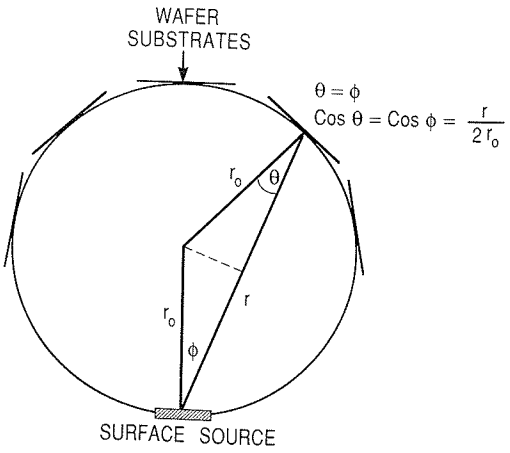

Figure 3-8. Evaporation scheme to achieve uniform deposition. Source and substrates lie on sphere of radius r_0.

cally, deposition uniformity is achieved because short source–substrate distances are offset by unfavorably large vapor emission and deposition angles. Alternately, long source–substrate distances are compensated by correspondingly small emission and reception angles. For sources with a higher degree of directionality (i.e., where $\cos^n\phi$ rather than $\cos\phi$ is involved), the reader can easily show that thickness uniformity is no longer maintained.

Two principal methods for optimizing film uniformity over large areas involve varying the geometric location of the source and interposing static as well as rotating shutters between evaporation sources and substrates. Computer calculations have proven useful in locating sources and designing shutter contours to meet the stringent demands of optical coatings. Film thickness uniformity cannot, however, be maintained beyond $\pm 1\%$ because of insufficient mechanical stability of both the stationary and rotating hardware.

In addition to the parallel source–substrate configuration, calculations of thickness distributions have also been made for spherical as well as conical, parabolic, and hyperbolic substrate surfaces (Ref. 9). Similarly, cylindrical, wire, and ring evaporation source geometries have been treated (Ref. 11). For the results, interested readers should consult the appropriate references.

3.3.3. Conformal Coverage

An issue related to film uniformity is step or, more generally, conformal coverage, and it arises primarily in the fabrication of integrated circuits. The required semiconductor contact and device interconnection metalization depositions frequently occur over a terrain of intricate topography where microsteps, grooves, and raised stripes abound. When the horizontal as well as vertical

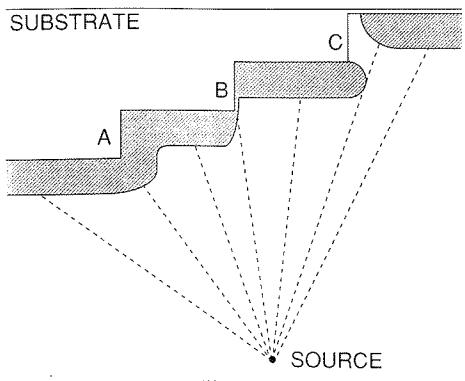

Figure 3-9. Schematic illustration of film coverage of stepped substrate: (A) uniform coverage; (B) poor sidewall coverage; (C) lack of coverage—discontinuous film.

surfaces of substrates are coated to the same thickness, we speak of conformal coverage. On the other hand, coverage will not be uniform when physical shadowing effects cause unequal deposition on the top and sidewalls of steps. Inadequate step coverage can lead to minute cracks in the metalization, which have been shown to be a major source of failure in device reliability testing. Thinned regions on conducting stripes exhibit greater Joule heating, which sometimes fosters early burnout. Step coverage problems have been shown to be related to the profile of the substrate step as well as to the evaporation source–substrate geometry. The simplest model of evaporation from a point source onto a stepped substrate results in either conformal coverage or a lack of deposition in the step shadow, as shown schematically in Fig. 3-9. Line-of-sight motion of evaporant atoms and sticking coefficients of unity can be assumed in estimating the extent of coverage.

More realistic computer modeling of step coverage has been performed for the case in which the substrate is located on a rotating planetary holder (Ref. 12). In Fig. 3-10 coverage of a 1-μm-wide, 1-μm-high test pattern with 5000 Å

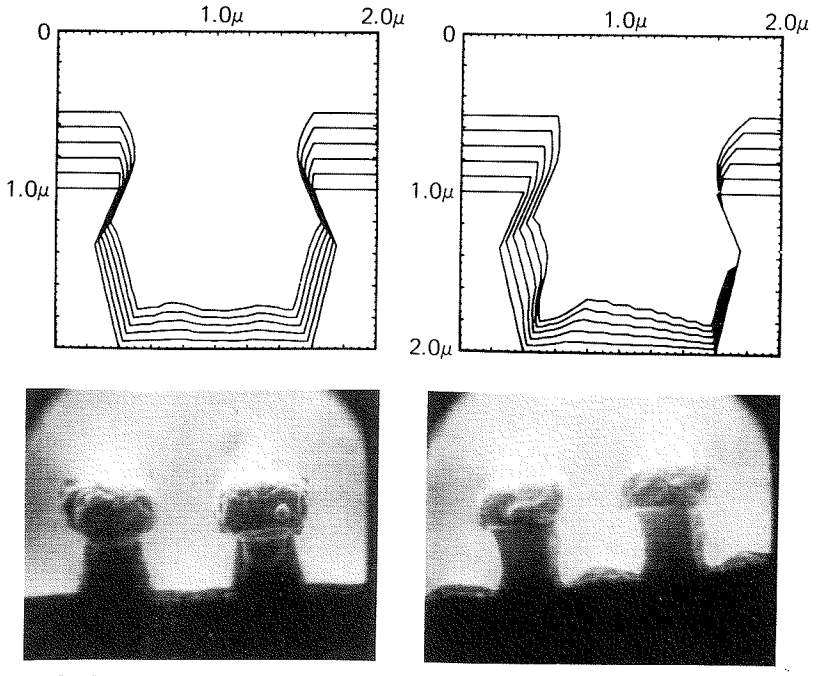

Figure 3-10. Comparison of simulated and experimental Al film coverage of 1-μm line step and trench features. (Left) Orientation of most symmetric deposition. (Right) Orientation of most asymmetric deposition. (Reprinted with permission from Cowan Publishing Co., from C. H. Ting and A. R. Neureuther, *Solid State Technology* **25**, 115, 1982).

of evaporated Al is simulated and compared with experiment. In the symmetric orientation the region between the pattern stripes always manages to "see" the source, and this results in a small plateau of full film thickness. In the asymmetric orientation, however, the substrate stripes cast a shadow with respect to the source biasing the deposition in favor of unequal sidewall coverage. In generating the simulated film profiles, the surface migration of atoms was neglected, a valid assumption at low substrate temperatures. Heating the substrate increases surface diffusion of depositing atoms, thus promoting the filling of potential voids as they form. Interestingly, similar step coverage problems exist in chemical-vapor-deposited SiO_2 and silicon nitride films.

3.3.4. Film Purity

The chemical purity of evaporated films depends on the nature and level of impurities that (1) are initially present in the source, (2) contaminate the source from the heater, crucible, or support materials, and (3) originate from the residual gases present in the vacuum system. In this section only the effect of residual gases on film purity will be addressed. During deposition the atoms and molecules of both the evaporant and residual gases impinge on the substrate in parallel, independent events. The evaporant vapor impingement rate is $\rho N_A \dot{d}/M_a$ atoms/cm^2-sec, where ρ is the density and $\dot{d}$ is the deposition rate (cm/sec). Simultaneously, gas molecules impinge at a rate given by Eq. 2-9. The ratio of the latter to the former is the impurity concentration C_i:

$$C_i = 5.82 \times 10^{-2} \frac{P}{\sqrt{M_g T}} \frac{M_a}{\rho \dot{d}}. \tag{3-21}$$

Terms M_a and M_g refer to evaporant and gas molecular weights, respectively, and P is the residual gas vapor pressure in torr.

Table 3-2 illustrates the combined role that deposition rate and residual pressure play in determining the oxygen level that can be incorporated into thin tin films (Ref. 13). Although the concentrations are probably overestimated because the sticking probabiltiy of O_2 is about 0.1 or less, the results have several important implications. To produce very pure films, it is important to deposit at very high rates while maintaining very low background pressures of residual gases such as H_2O, CO_2, CO, O_2, and N_2. Neither of these requirements is too formidable for vacuum evaporation, where deposition rates from electron-beam sources can reach 1000 Å/sec at chamber pressures of $\sim 10^{-8}$ torr.

On the other hand, in sputtering processes, discussed later in the chapter,

Table 3-2. Maximum Oxygen Concentration in Tin Films Deposited at Room Temperature

P_{O_2} (torr)	Deposition Rate (A/sec)			
	1	10	100	1000
10^{-9}	10^{-3}	10^{-4}	10^{-5}	10^{-6}
10^{-7}	10^{-1}	10^{-2}	10^{-3}	10^{-4}
10^{-5}	10	1	10^{-1}	10^{-2}
10^{-3}	10^{3}	10^{2}	10	1

From Ref. 13.

deposition rates are typically more than an order of magnitude less, and chamber pressures five orders of magnitude higher than for evaporation. Therefore, the potential exists for producing films containing high gas concentrations. For this reason sputtering was traditionally not considered to be as "clean" a process as evaporation. Considerable progress has been made in the last two decades, however, with the commercial development of high-deposition-rate magnetron sputtering systems, operating at somewhat lower gas pressures in cleaner vacuum systems. In the case of aluminum films, comparable purities appear to be attained in both processes. Lastly, Table 3-2 suggests that very high oxygen incorporation occurs at residual gas pressures of 10^{-3} torr. Advantage of this fact is taken in reactive evaporation processes where intentionally introduced gases serve to promote reactions with the evaporant metal and control the deposit stoichiometry.

The presence of gaseous impurities within metal films sometimes has a pronounced effect in degrading many of its properties. Oxygen and nitrogen incorporation has been observed to reduce both the electrical conductivity and optical reflectivity as well as increase the hardness of Al films (Ref. 14).

3.4. Evaporation Hardware and Techniques

3.4.1. Resistance-Heated Evaporation Sources

This section will primarily be devoted to a brief description of the most widely used methods for heating evaporants. Clearly, heaters must reach the temperature of the evaporant in question while having a negligible vapor pressure in comparison. Ideally, they should not contaminate, react, or alloy with the evaporant or release gases such as oxygen, nitrogen, or hydrogen at the evaporation temperature. These requirements have led to the development and use of suitable resistance and electron-beam-heated sources.

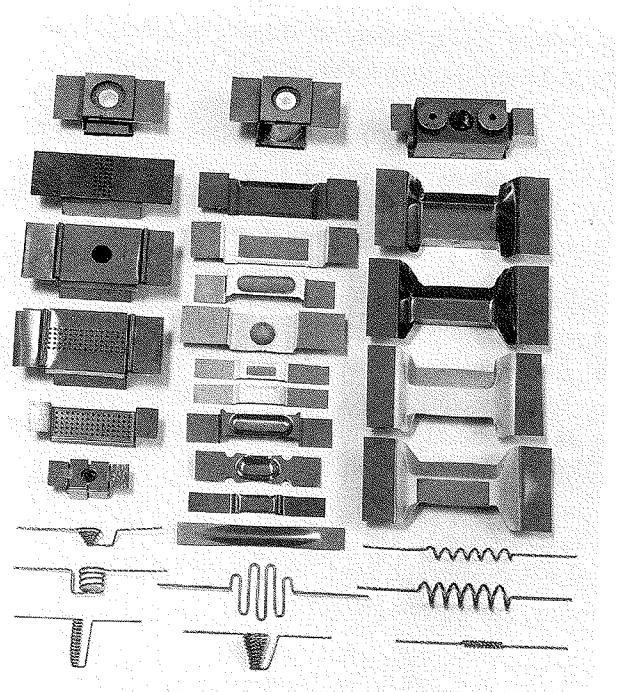

Figure 3-11. Assorted resistance heated evaporation sources. (Courtesy of R. D. Mathis Company).

Resistively heated evaporation sources are available in a wide variety of forms utilizing refractory metals singly or in combination with inert oxide or ceramic compound crucibles. Some of these are shown in Fig. 3-11. They can be divided into the following important categories.

3.4.1.1. Tungsten Wire Sources. Tungsten wire sources are in the form of individual or multiply stranded wires twisted into helical or conical shapes. Helical coils are used for metals that wet tungsten readily, whereas the conical baskets are better adapted to contain poorly wetting materials. In the former case, metal evaporant wire is wrapped around or hung from the tungsten strands, and the molten beads of metal are retained by surface tension forces.

3.4.1.2. Refractory Metal Sheet Sources. Tungsten, tantalum, and molybdenum sheet metal sources, like the wire filaments, are self-resistance

heaters that require low-voltage, high-current power supplies. These sources have been fabricated into a variety of shapes, including dimpled strip, boat, canoe, and deep-folded configurations. Folded boat sources have been used to evaporate MgF_2 by containing the bulk salt and melting it prior to vaporization. Powder mixtures of metals and metal oxides used for coating ophthalmic lenses have been similarly evaporated from deep-folded boats in batch-type evaporators.

3.4.1.3. Sublimation Furnaces. Efficient evaporation of sulfides, selenides, and some oxides is carried out in sublimation furnaces. The evaporant materials in powder form are pressed and sintered into pellets and heated by surrounding radiant heating sources. Spitting and ejection of particles caused by evolution of gases occluded within the source compacts are avoided through the use of baffled heating assemblies. These avoid direct line-of-sight access to substrates, and evaporation rates from such sources tend to be constant over extended periods of time. The furnaces are typically constructed of sheet tantalum, which is readily cut, bent, and spot-welded to form heaters, radiation shields, supports, and current bus strips.

3.4.1.4. Crucible Sources. The most common sources are cylindrical cups composed of oxides, pyrolytic BN, graphite, and refractory metals, which are fabricated by hot-pressing powders or machining bar stock. These crucibles are normally heated by external tungsten wire heating elements wound to fit snugly around them.

Other crucible sources rely on high-frequency induction rather than resistance heating. In a configuration resembling a transformer, high-frequency currents are induced in either a conducting crucible or evaporant charge serving as the secondary, resulting in heating. The powered primary is a coil of water-cooled copper tubing that surrounds the crucible. Aluminum evaporated from BN or BN/TiB_2 composite crucibles, in order to metalize integrated circuits, is an important example of the use of induction heating.

Another category of crucible source consists of a tungsten wire resistance heater in the form of a conical basket encased in Al_2O_3 or refractory oxide to form an integral crucible–heater assembly. Such crucibles frequently serve as evaporant sources in laboratory scale film deposition systems.

3.4.2. Electron-Beam Evaporation

Disadvantages of resistively heated evaporation sources include possible contamination by crucibles, heaters, and support materials and the limitation of

relatively low input power levels. This makes it difficult to deposit pure films or evaporate high-melting-point materials at appreciable rates. Electron-beam heating eliminates these disadvantages and has, therefore, become the most widely used vacuum evaporation technique for preparing highly pure films. In principle, this type of source enables evaporation of virtually all materials at almost any rate. As shown in Fig. 3-12, the evaporant charge is placed in either a water-cooled crucible or in the depression of a water-cooled copper hearth. The purity of the evaporant is ensured because only a small amount of charge melts or sublimes so that the effective crucible is the unmelted skull material next to the cooled hearth. For this reason there is no contamination of the evaporant by Cu. Multiple-source units are available for the sequential or parallel deposition of more than one material.

In the most common configuration of the gun source, electrons are thermionically emitted from heated filaments, which are shielded from direct line of sight of the evaporant charge and substrate. Film contamination from the heated electron source is eliminated in this way. The filament cathode assembly potential is biased negatively with respect to a nearby grounded anode by anywhere from 4 to 20 kV, and this serves to accelerate the electrons. In addition, a transverse magnetic field is applied, which serves to deflect the electron beam in a 270° circular arc and focus it on the hearth and evaporant charge at ground potential. The reader can verify the electron trajectory through the use of the right-hand rule. This states that if the thumb is in the direction of the initial electron emission, and the forefinger lies in the direction of the magnetic field (north to south), then the middle finger indicates the direction of the force on the electron and its resultant path at any instant.

It is instructive to estimate the total power that must be delivered by the electron beam to the charge in order to compensate for the following heat losses incurred during evaporation of 10^{18} atoms/cm^2-sec (Ref. 5).

1. The power density P_s (watts/cm^2) that must be supplied to account for the heat of sublimation ΔH_s (eV) is

$$P_s = 10^{18}(1.6 \times 10^{-19})\,\Delta H_s = 0.16\,\Delta H_s. \qquad (3\text{-}22a)$$

2. The kinetic energy of evaporant is $(3/2)kT_s$ per atom so that the required power density P_k is

$$P_k = 10^{18}\,(3/2)(1.38 \times 10^{-23})T_s = 2.07 \times 10^{-5}T_s, \quad (3\text{-}22b)$$

where T_s is the source temperature.

3. The radiation heat loss density is

$$P_r = 5.67 \times 10^{-12}\varepsilon(T_s^4 - T_0^4), \qquad (3\text{-}22c)$$

where ε is the source emissivity at T_s, and $T_0 \approx 293$ K.

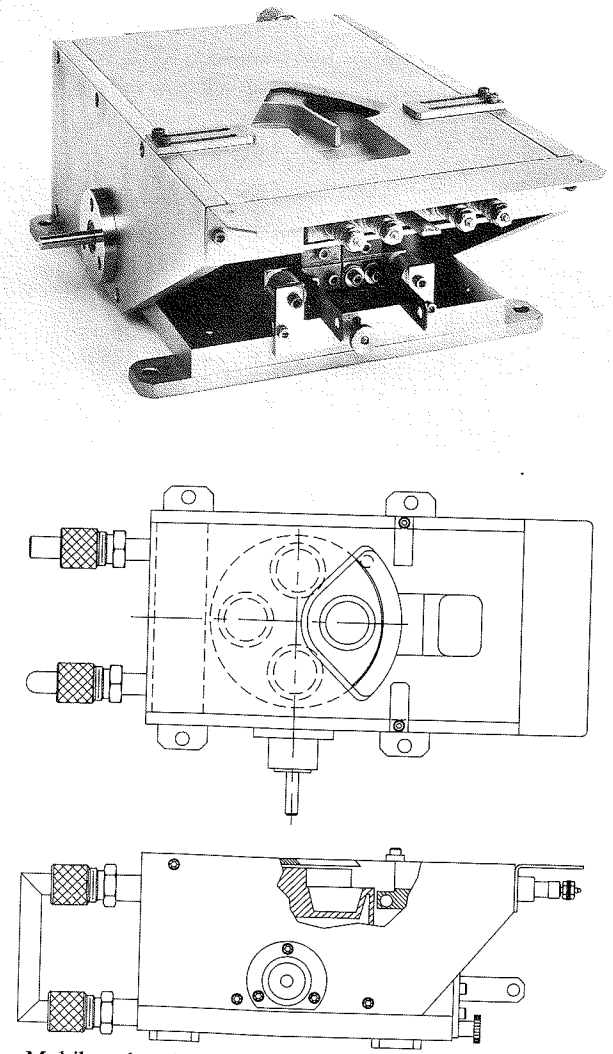

Figure 3-12. Multihearth electron beam evaporation unit with accompanying schematics. (Courtesy of Temescal unit of Edwards High Vacuum International, a division of the BOC Group, Inc.).

4. Heat conduction through a charge of thickness l into the hearth dissipates a power density P_c equal to

$$P_c = \kappa\left(\frac{T_s - T_0}{l}\right), \tag{3-22d}$$

where κ is the thermal conductivity of the charge. For the case of Au at T_s = 1670 K, where $\Delta H_s \approx 3.5$ eV, $\varepsilon \sim 0.4$, $l = 1$ cm, and $\kappa = 3.1$ W/cm-K, the corresponding values are $P_s = 0.56$ W/cm^2, $P_k = 0.034$ W/cm^2, P_r = 17.6 W/cm^2, and $P_c = 4.3$ kW/cm^2. Clearly the overwhelming proportion of the power delivered by the electron beam is conducted through the charge to the hearth. In actuality, power densities of ~ 10 kW/cm^2 are utilized in melting metals, but such levels would damage dielectrics, which require perhaps only 1–2 kW/cm^2. To optimize evaporation conditions, provision is made for altering the size of the focal spot and for electromagnetically scanning the beam.

3.4.3. Deposition Techniques

By now, films of virtually all important materials have been prepared by physical vapor deposition techniques. A practical summary (Refs. 15–17) of vacuum evaporation methods is given in Table 3-3, where recommended heating sources and crucible materials are listed for a number of metals, alloys, oxides, and compounds. Prior to settling on a particular vapor phase deposition process, both PVD and CVD options should be investigated together with the numerous hybrid variants of these methods (see Section 3.8). Paramount attention should be paid to film quality and properties, and the requirements and costs necessary to achieve them. If, after all, vacuum evaporation is selected, modestly equipped laboratories may wish to consider the resistively heated sources before the more costly electron-beam or induction heating alternatives.

3.5. Glow Discharges and Plasmas

3.5.1. Introduction

A perspective of much of the contents of the remainder of the chapter can be had by considering the simplified sputtering system shown in Fig. 3-13a. The target is a plate of the materials to be deposited or the material from which a film is synthesized. Because it is connected to the negative terminal of a dc or RF power supply, the target is also known as the cathode. Typically, several

Table 3-3. Evaporation Characteristics of Materials

Material	Minimum[a] Evap. Temp	State of Evaporation	Recommended Crucible Material	e-beam[b] Deposition Rate (Å/s)	e-beam[b] Power (kW)
Aluminum	1010	Melts	BN	20	5
Aluminum oxide	1325	Semimelts		10	0.5
Antimony	425	Melts	BN, Al_2O_3	50	0.5
Arsenic	210	Sublimes	Al_2O_3	100	0.1
Beryllium	1000	Melts	Graphite, BeO	100	1.5
Beryllium oxide		Melts		40	1.0
Boron	1800	Melts	Graphite, WC	10	1.5
Boron carbide		Semimelts		35	1.0
Cadmium	180	Melts	Al_2O_3, quartz	30	0.3
Cadmium sulfide	250	Sublimes	Graphite	10	0.25
Calcium fluoride		Semimelts		30	0.05
Carbon	2140	Sublimes		30	1.0
Chromium	1157	Sublimes	W	15	0.3
Cobalt	1200	Melts	Al_2O_3, B_2O_3	20	2.0
Copper	1017	Melts	Graphite, Al_2O_3	50	0.2
Gallium	907	Melts	Al_2O_3, graphite		
Germanium	1167	Melts	Graphite	25	3.0
Gold	1132	Melts	Al_2O_3, BN	30	6.0
Indium	742	Melts	Al_2O_3	100	0.1
Iron	1180	Melts	Al_2O_3, B_2O_3	50	2.5
Lead	497	Melts	Al_2O_3	30	0.1
Lithium fluoride	1180	melts (viscous)	Mo, W	10	0.15
Magnesium	327	sublimes	graphite	100	0.04
Magnesium fluoride	1540	semimelts	Al_2O_3	30	0.01
Molybdenum	2117	melts		40	4.0
Nickel	1262	melts	Al_2O_3, B_2O_3	25	2.0
Permalloy	1300	melts	Al_2O_3	30	2.0
Platinum	1747	melts	graphite	20	4.0
Silicon	1337	melts	B_2O_3	15	0.15
Silicon dioxide	850	semimelts	Ta	20	0.7

[a]Temperature (°C) at which vapor pressure is 10^{-4} torr.
[b]For 10 kV, copper hearth, source–substrate distance of 40 cm.
Adapted from Refs. 16 and 17.

Table 3-3. *Continued.*

Material	Minimum[a] Evap. Temp	State of Evaporation	Recommended Crucible Material	e-beam[b] Deposition Rate (Å/s)	e-beam[b] Power (kW)
Silicon monoxide	600	sublimes	Ta	20	0.1
Tantalum	2590	semimelts		100	5.0
Tin	997	melts	Al_2O_3, graphite	10	2.0
Titanium	1453	melts		20	1.5
Titanium dioxide	1300	melts	W	10	1.0
Tungsten	2757	melts		20	5.5
Zinc	250	sublimes	Al_2O_3	50	0.25
Zinc selenide	660	sublimes	quartz		
Zinc sulfide	300	sublimes	Mo		
Zirconium	1987	melts	W	20	5.0

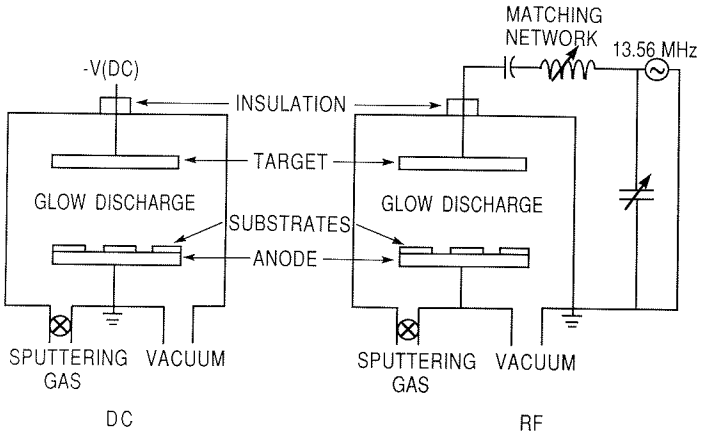

Figure 3-13. Schematics of simplified sputtering systems: (a) dc, (b) RF.

kilovolts are applied to it. The substrate that faces the cathode may be grounded, electrically floating, biased positively or negatively, heated, cooled, or some combination of these. After evacuation of the chamber, a gas, typically argon, is introduced and serves as the medium in which a discharge is initiated and sustained. Gas pressures usually range from a few to 100 mtorr. After a visible glow discharge is maintained between the electrodes, it is observed that a current flows and that a film condenses on the substrate

(anode). In vacuum, of course, there is no current flow and no film deposition. Microscopically, positive ions in the discharge strike the cathode plate and eject neutral target atoms through momentum transfer. These atoms enter and pass through the discharge region to eventually deposit on the growing film. In addition, other particles (secondary electrons, desorbed gases, and negative ions) as well as radiation (X-rays and photons) are emitted from the target. In the electric field the negatively charged ions are accelerated toward the substrate to bombard the growing film.

From this simple description, it is quite apparent that compared to the predictable rarefied gas behavior in an evaporation system, the glow discharge is a very busy and not easily modeled environment. Regardless of the type of sputtering, however, roughly similar discharges, electrode configurations, and gas–solid interactions are involved. Therefore, issues common to all glow discharges will be discussed prior to the detailed treatment required of specific sputtering processes and applications.

3.5.2. DC Glow Discharges

The manner in which a glow discharge progresses in a low-pressure gas using a high-impedance dc power supply is as follows (Refs. 4–6). A very small current flows at first due to the small number of initial charge carriers in the system. As the voltage is increased, sufficient energy is imparted to the charged particles to create more carriers. This occurs through ion collisions with the cathode, which release secondary electrons, and by impact ionization of neutral gas atoms. With charge multiplication, the current increases rapidly, but the voltage, limited by the output impedance of the power supply, remains constant. This regime is known as the Townsend discharge. Large numbers of electrons and ions are created through avalanches. Eventually, when enough of the electrons generated produce sufficient ions to regenerate the same number of initial electrons, the discharge becomes self-sustaining. The gas begins to glow now, and the voltage drops, accompanied by a sharp rise in current. At this state "normal glow" occurs. Initially, ion bombardment of the cathode is not uniform but is concentrated near the cathode edges or at other surface irregularities. As more power is applied, the bombardment increasingly spreads over the entire surface until a nearly uniform current density is achieved. A further increase in power results in higher voltage and current density levels. The "abnormal discharge" regime has now been entered, and this is the operative domain for sputtering and other discharge processes (e.g., plasma etching of thin films). At still higher currents, low-voltage arcs propagate.

Adjacent to the cathode there is a highly luminous layer known as the

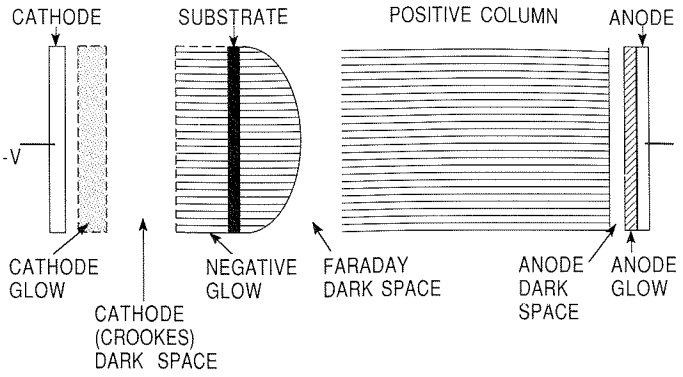

Figure 3-14. Luminous regions of the dc glow discharge.

cathode glow. The light emitted depends on the incident ions and the cathode material. In the cathode glow region, neutralization of the incoming discharge ions and positive cathode ions occurs. Secondary electrons start to accelerate away from the cathode in this area and collide with neutral gas atoms located some distance away from the cathode. In between is the Crookes dark space, a region where nearly all of the applied voltage is dropped. Within the dark space the positive gas ions are accelerated toward the cathode.

The next distinctive region is the "negative glow," where the accelerated electrons acquire enough energy to impact-ionize the neutral gas molecules. Beyond this is the Faraday dark space and finally the positive column. The sequence of these discharge regimes is schematically depicted in Fig. 3-14. The substrate (anode) is placed inside the negative glow, well before the Faraday dark space so that the latter as well as the positive column do not normally appear during sputtering.

3.5.3. Discharge Species (Ref. 6)

A discharge is essentially a plasma—i.e., a partially ionized gas composed of ions, electrons, and neutral species that is electrically neutral when averaged over all the particles contained within. Moreover, the density of charged particles must be large enough compared with the dimensions of the plasma so that significant Coulombic interaction occurs. This interaction enables the charged species to behave in a fluidlike fashion and determines many of the plasma properties. The plasmas used in sputtering are called glow discharges. In them the particle density is low enough, and the fields are sufficiently strong so that neutrals are not in equilibrium with electrons. Typically, the degree of ionization or ratio between numbers of ions and neutrals is about 10^{-4}.

Therefore, at pressures of 10 mtorr, the perfect gas law indicates that about 3×10^9 ions as well as electrons/cm^3 will be present at 25°C. Measurements on glow discharges yield average electron energies of about 2 eV. The effective temperature T associated with a given energy E is simply given by $T = E/k$, where k is the Boltzmann constant. Substituting, we find that electrons have an astoundingly high temperature of some 23,000 K. However, because there are so few of them, their heat content is small and the chamber walls do not heat appreciably. Neutrals and ions are not nearly as energetic; the former have energies of only 0.025 eV (or $T = 290$ K) and the latter, energies of ~ 0.04 eV (or $T = 460$ K). Ions have higher energies than neutrals because they acquire energy from the applied electric field.

Since surfaces (e.g., targets, substrates) are immersed in the plasma, they are bombarded by the species present. The neutral particle flux can be calculated from Eq. 2-8. Charged particle impingement results in an effective current density J_i given by the product of the particle flux and the charge q_i transported. Therefore,

$$J_i = n_i q_i \bar{v}_i / 4, \tag{3-23}$$

where n_i and $\bar{v}_i$ are the specie concentration and mean velocity, respectively. By Eq. 2-3b, $\bar{v}_i = (8kT/\pi m)^{1/2}$. For electrons $m = 9.1 \times 10^{-28}$ g, and if we assume $T = 23{,}000$ K and $n = 10^{10}$/cm^3, $J_{\text{electron}} \sim 38$ mA/cm^2. The ions, present in the same amounts as electrons, are much heavier and have a lower effective temperature than the electrons. This accounts for their very low velocity compared with that of electrons. For example, $\bar{v}_{\text{ion}} = 5.2 \times 10^4$ cm/sec for Ar ions as well as neutral atoms, whereas for electrons $\bar{v}_{\text{electron}} = 9.5 \times 10^7$ cm/sec. The ion current is correspondingly reduced relative to the electron current by the ratio of these velocities, so $J_{\text{ion}} = 21\ \mu$A/cm^2.

The implication of this simple calculation is that an isolated surface within the plasma charges negatively initially. Subsequently, additional electrons are repelled and positive ions are attracted. Therefore, the surface continues to charge negatively at a decreasing rate until the electron flux equals the ion flux and there is no net steady-state current. We can then expect that both the anode and cathode in the glow discharge will be at a negative potential with respect to the plasma. Of course, the application of the large external negative potential alters the situation, but the voltage distribution in a dc glow discharge under these conditions is shown schematically in Fig. 3-15. A sheath develops around each electrode with a net positive space charge. The lower electron density in the sheath means less ionization and excitation of neutrals. Hence, there is less luminosity there than in the glow itself. Electric fields (derivative of the potential) are restricted to the sheath regions. The plasma itself is not at a

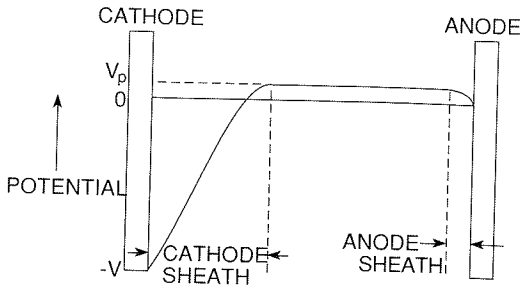

Figure 3-15. Voltage distribution across dc glow discharge.

potential intermediate between that of the electrodes but is typically some 10 V positive with respect to the anode at zero potential. Sheath width dimensions depend on the electron density and temperature. Using the values given earlier for the electrically isolated surface, we find that the sheath width is about 100 μm. It is at the sheath–plasma interface that ions begin to accelerate on their way to the target during sputtering; electrons, however, are repelled from both sheath regions. All of these unusual charge effects stem from the fact that the fundamental plasma particles (electrons and ions) have such different masses and, hence, velocities and energies.

3.5.4. Collision Processes

Collisions between electrons and all the other species (charged or neutral) within the plasma dominate the properties of the glow discharge. Collisions are elastic or inelastic, depending on whether the internal energy of the colliding specie is preserved. In an elastic collision, exemplified by the billiard ball analogy of elementary physics, only kinetic energy is interchanged, and we speak of conservation of momentum and *kinetic* energy of translational motion. The *potential* energy basically resides within the electronic structure of the colliding ions, atoms, and molecules, etc., and increases in potential energy are manifested by ionization or other excitation processes. In an elastic collision, no atomic excitation occurs and potential energy is conserved. This is the reason why only kinetic energy is considered in the calculation. The well-known result for elastic binary collisions is

$$\frac{E_2}{E_1} = \frac{4M_1M_2}{(M_1 + M_2)^2}\cos^2\theta, \qquad (3\text{-}24)$$

where 1 and 2 refer to the two particles of mass M_i and energy E_i. We assume M_2 is initially stationary and M_1 collides with it at an angle θ defined by the

initial trajectory and the line joining their centers at contact. The quantity $4M_1M_2/(M_1 + M_2)^2$ is known as the energy transfer function. When $M_1 = M_2$, it has a value of 1; i.e., after collision the initial moving projectile remains stationary, and all of its energy is efficiently transferred to the second particle, which speeds away. When, however, $M_1 \ll M_2$, reflecting, say, a collision between a moving electron and a stationary nitrogen molecule, then the energy transfer function is $\sim 4M_1/M_2$ and has a typical value of $\sim 10^{-4}$. Little kinetic energy is transferred in the collision of the light electron with the massive nitrogen atom.

Now consider inelastic collisions. The change in internal energy, ΔU, of the struck particle must now be accounted for in the condition requiring conservation of total energy. It is left as an exercise for the reader to demonstrate that the maximum fraction of kinetic energy transferred is given by

$$\frac{\Delta U}{(1/2)M_1v_1^2} = \frac{M_2}{M_1 + M_2}\cos^2\theta, \tag{3-25}$$

where v_1 is the initial velocity of particle 1. For the inelastic collision between an electron and nitrogen molecule, $\Delta U/(1/2)M_1v_1^2 \approx 1$, when $\cos\theta = 1$. Therefore, contrary to an elastic collision, virtually all of an electron's kinetic energy can be transferred to the heavier species in the inelastic collision.

We now turn our attention to a summary of the rich diversity of inelastic collisions and chemical processes that occur in plasmas. It is well beyond the scope of this book to consider anything beyond a cataloging of reactions (Ref. 6). Suffice it to say that these reactions generally enhance film deposition and etching processes.

1. Ionization. The most important process in sustaining the discharge is electron impact ionization. A typical reaction is

$$e^- + Ar^\circ \rightarrow Ar^+ + 2e^-. \tag{3-26a}$$

The two electrons can now ionize more Ar°, etc. By this multiplication mechanism the glow discharge is sustained. The reverse reaction, in which an electron combines with the positive ion to form a neutral, also occurs and is known as recombination.

2. Excitation. In this case the energy of the electron excites quantitized transitions between vibrational, rotational, and electronic states, leaving the molecule in an excited state (denoted by an asterisk). An example is

$$e^- + O_2{}^\circ \rightarrow O_2^* + e^-. \tag{3-26b}$$

3. Dissociation. In dissociation the molecule is broken into smaller atomic or molecular fragments. The products (radicals) are generally much more

chemically active than the parent gas molecule and serve to accelerate reactions. Dissociation of CF_4, for example, is relied on in plasma etching or film removal processes; i.e.,

$$e^- + CF_4 \rightarrow e^- + CF_3^* + F^*. \quad (3\text{-}26c)$$

4. Dissociative Ionization. During dissociation one of the excited species may become ionized; e.g.,

$$e^- + CF_4 \rightarrow 2e^- + CF_3^+ + F^*. \quad (3\text{-}26d)$$

5. Electron Attachment. Here neutral molecules become negative ions after capturing an electron. For example,

$$e^- + SF_6^\circ \rightarrow SF_6^-. \quad (3\text{-}26e)$$

6. Dissociative Attachment.

$$e^- + N_2^\circ \rightarrow N^+ + N^- + e^-. \quad (3\text{-}26f)$$

In addition to electron collisions, ion–neutral as well as excited or metastable–excited, and excited atom–neutral collisions occur. Some generic examples of these reactions are as follows:

7. Symmetrical Charge Transfer.

$$A + A^+ \rightarrow A^+ + A.$$

8. Asymmetric Charge Transfer.

$$A + B^+ \rightarrow A^+ + B.$$

9. Metastable–Neutral.

$$A^* + B \rightarrow B^+ A + e^-.$$

10. Metastable–Metastable Ionization.

$$A^* + A^* \rightarrow A + A^+ + e^-.$$

Evidence for these uncommon gas-phase species and reactions has accumulated through real-time monitoring of discharges by mass as well as light emission spectroscopy. As a result, a remarkable picture of plasma chemistry has emerged. For example, a noble gas like Ar when ionized loses an electron and resembles Cl electronically as well as chemically. The fact that these species are not in equilibrium confounds the thermodynamic and kinetic descriptions of these reactions.

3.6. Sputtering

3.6.1. Ion – Surface Interactions

Critical to the analysis and design of sputtering processes is an understanding of what happens when ions collide with surfaces (Ref. 18). Some of the

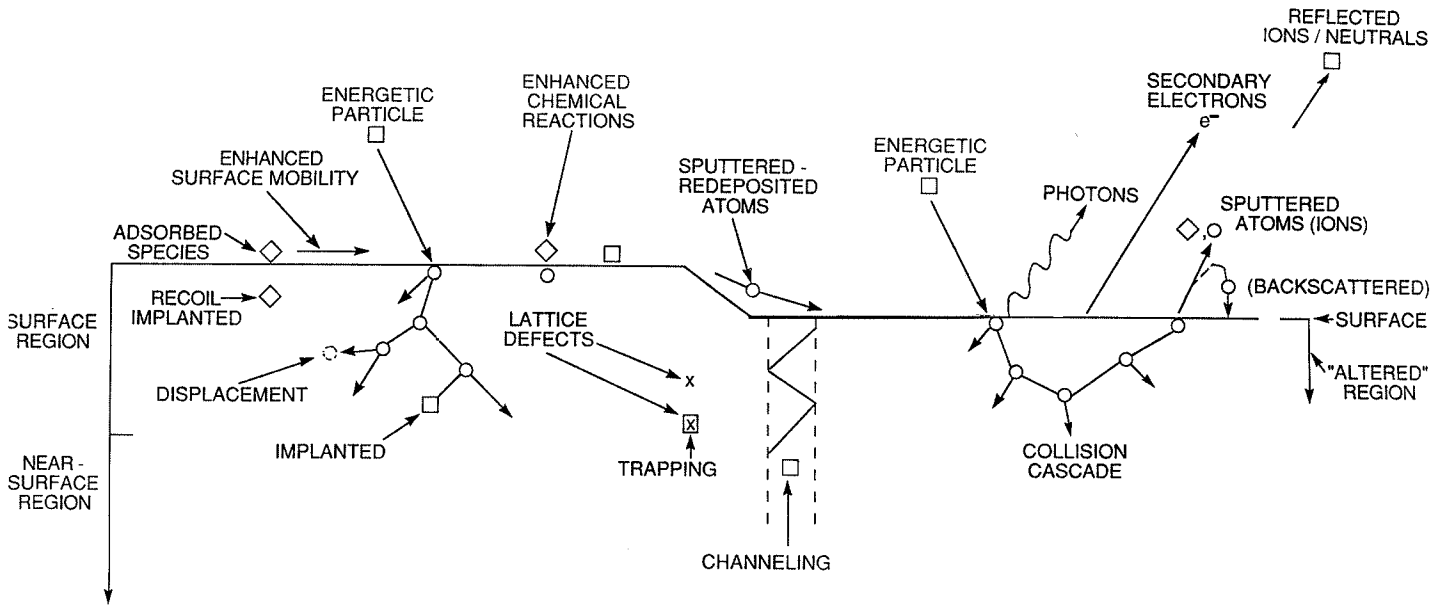

Figure 3-16. Depiction of energetic particle bombardment effects on surfaces and growing films. (From Ref. 18).

interactions that occur are shown schematically in Fig. 3-16. Each depends on the type of ion (mass, charge), the nature of surface atoms involved, and, importantly, on the ion energy. Several of these interactions have been capitalized upon in widely used thin-film processing, deposition, and characterization techniques. For example, ion implantation involves burial of ions under the target surface. Ion implantation of dopants such as B, P, As into Si wafers at ion energies ranging from tens to 100 keV is essential in the fabrication of devices in very large scale integrated (VLSI) circuits. Even higher energies are utilized to implant dopants into GaAs matrices. Ion fluxes, impingement times, and energies must be precisely controlled to yield desired doping levels and profiles. In contrast, ion-scattering spectroscopy techniques require that the incident ions be reemitted for measurement of energy loss. Rutherford backscattering (RBS) is the most important of these analytical methods and typically relies on 2-MeV He^+ ions. Through measurement of the intensity of the scattered ion signal, it is possible to infer the thickness and composition of films as well as subsurface compound layers. This subject is treated at length in Chapter 6. Secondary electrons as well as the products of core electron excitation—Auger electrons, X-rays, etc.—also form part of the complement of particles and radiation leaving the surface.

3.6.2. Sputter Yield

When the ion impact establishes a train of collision events in the target leading to the ejection of a matrix atom, we speak of sputtering. An impressive body of literature has been published indicating that sputtering is related to momentum transfer from energetic particles to the surface atoms of the target. Sputtering has, therefore, been aptly likened to "atomic pool" where the ion (cue ball) breaks up the close-packed rack of atoms (billiard balls), scattering some backward (toward the player). Even though atoms of a solid are bound to one another by a complex interatomic potential, whereas billiard balls do not interact, sputtering theory uses the idea of elastic binary collisions. Theoretical expressions for the sputter yield S, the most fundamental parameter characterizing sputtering, include the previously introduced energy transfer function. The sputter yield is defined as the number of atoms or molecules ejected from a target surface per incident ion and is a measure of the efficiency of sputtering.

Intuitively we expect S to be proportional to a product of the following factors (Ref. 19):

1. The number of atoms displaced toward the surface per primary collision. This term is given by $\overline{E}/2E_t$, where $\overline{E}$ is the mean energy of the struck

target atom and E_t is the threshold energy required to displace an atom. The factor of 2 is necessary because only half of the displaced atoms move toward the surface. The quantity $\bar{E}$ may be taken as an average of E_2, the kinetic energy transferred to the target atom, and E_t; i.e.,

$$\bar{E} = \frac{E_2 + E_t}{2}, \qquad \text{where } E_2 = \frac{4M_1M_2}{(M_1 + M_2)^2}E_1.$$

2. The number of atomic layers that contain these atoms and contribute to sputtering. Statistics show that the number of collisions required to slow an atom of energy $\bar{E}$ to E_b, the surface binding energy, is

$$N = \frac{\ln \bar{E}/E_b}{\ln 2}. \tag{3-27}$$

   By a random walk model, the average number of contributing atomic layers is $1 + N^{1/2}$.
3. The number of target atoms per unit area n_A.
4. The cross section $\sigma_0 = \pi a^2$, where a is related to the Bohr radius of the atom a_b, and the atomic numbers Z_1, Z_2 of the incident ion and sputtered atom respectively; i.e.,

$$a = \frac{a_b}{\sqrt{Z_1^{2/3} + Z_2^{2/3}}}.$$

   Combining terms gives

$$S = \frac{\bar{E}}{4E_t}\left\{1 + \left(\frac{\ln \bar{E}/E_b}{\ln 2}\right)^{1/2}\right\}\sigma_0 n_A. \tag{3-28}$$

As an example consider the sputtering of Cu with 1-keV Ar ions. The calculated value of S will depend strongly on E_t, and for Ar incident on Cu experiment suggests that $E_t = 17$ eV. For Cu, $M_2 = 63.5$, $Z_2 = 29$, $a_b = 1.17$ Å, $n_A = 1.93 \times 10^{15}$ atoms/cm^2, and $E_b = 3.5$ eV. For Ar, $M_1 = 39.9$ and $Z_1 = 18$. Substitution shows that $\bar{E} = 483$ eV and $S = 1.3$. This calculated value compares with the measured sputter yield of 2.85, as indicated by the data of Table 3-4.

The currently accepted theory for the sputtering yield from collision cascades is due to Sigmund (Ref. 20) and predicts that

$$S = \frac{3\alpha}{4\pi^2}\frac{4M_1M_2}{(M_1 + M_2)^2}\frac{E_1}{E_b} \qquad (E_1 < 1 \text{ keV}) \tag{3-29}$$

Table 3-4. Sputtering Yield Data for Metals (atoms/ion)

Sputtering Gas	He	Ne	Ar	Kr	Xe	Ar	Ar Threshold
Energy (keV)	0.5	0.5	0.5	0.5	0.5	1.0	Voltage (eV)
Ag	0.20	1.77	3.12	3.27	3.32	3.8	15
Al	0.16	0.73	1.05	0.96	0.82	1.0	13
Au	0.07	1.08	2.40	3.06	3.01	3.6	20
Be	0.24	0.42	0.51	0.48	0.35		15
C	0.07	—	0.12	0.13	0.17		
Co	0.13	0.90	1.22	1.08	1.08		25
Cu	0.24	1.80	2.35	2.35	2.05	2.85	17
Fe	0.15	0.88	1.10	1.07	1.00	1.3	20
Ge	0.08	0.68	1.1	1.12	1.04		25
Mo	0.03	0.48	0.80	0.87	0.87	1.13	24
Ni	0.16	1.10	1.45	1.30	1.22	2.2	21
Pt	0.03	0.63	1.40	1.82	1.93		25
Si	0.13	0.48	0.50	0.50	0.42	0.6	
Ta	0.01	0.28	0.57	0.87	0.88		26
Ti	0.07	0.43	0.51	0.48	0.43		20
W	0.01	0.28	0.57	0.91	1.01		33

From Refs. 4 and 6.

and

$$S = 3.56\alpha \frac{Z_1 Z_2}{Z_1^{2/3} + Z_2^{2/3}} \left(\frac{M_1}{M_1 + M_2} \right) \frac{S_n(E)}{E_b} \qquad (E_1 > 1 \text{ keV}). \quad (3\text{-}30)$$

These equations depend on two complex quantities, α and $S_n(E)$. The parameter α, a measure of the efficiency of momentum transfer in collisions, increases monotonically from 0.17 to 1.4 as M_1/M_2 ranges from 0.1 to 10. The reduced stopping power, $S_n(E)$, is a measure of the energy loss per unit length due to nuclear collisions. It is a function of the energy as well as masses and atomic numbers of the atoms involved. At high energy, S is relatively constant because $S_n(E)$ tends to be independent of energy.

The sputter yields for a number of metals are entered in Table 3-4. Values for two different energies (0.5 keV and 1.0 keV) as well as five different inert gases (He, Ne, Ar, Kr, and Xe) are listed. It is apparent that S values typically span a range from 0.01 to 4 and increase with the mass and energy of the sputtering gas.

3.6.3. Sputtering of Alloys

In contrast to the fractionation of alloy melts during evaporation, with subsequent loss of deposit stoichiometry, sputtering allows for the deposition of

films having the same composition as the target source. This is the primary reason for the widespread use of sputtering to deposit metal alloy films. We note, however, that each alloy component evaporates with a different vapor pressure and sputters with a different yield. Why then is film stoichiometry maintained during sputtering and not during evaporation? One reason is the generally much greater disparity in vapor pressures compared with the difference in sputter yields under comparable deposition conditions. Second, and perhaps more significant, melts homogenize readily due to rapid atomic diffusion and convection effects in the liquid phase; during sputtering, however, minimal solid-state diffusion enables the maintenance of the required altered target surface composition.

Consider now sputtering effects (Ref. 5) on a binary alloy target surface containing a number of A atoms (n_A) and B atoms (n_B), such that the total number is $n = n_A + n_B$. The target concentrations are $C_A = n_A/n$ and $C_B = n_B/n$, with sputter yields S_A and S_B. Initially, the ratio of the sputtered atom fluxes (ψ) is given by

$$\frac{\psi_A}{\psi_B} = \frac{S_A C_A}{S_B C_B}. \tag{3-31}$$

If n_g sputtering gas atoms impinge on the target, the total number of A and B atoms ejected are $n_g C_A S_A$ and $n_g C_B S_B$, respectively. Therefore, the target surface concentration ratio is modified to

$$\frac{C'_A}{C'_B} = \frac{C_A}{C_B}\frac{(1 - n_g S_A/n)}{(1 - n_g S_B/n)} \tag{3-32}$$

instead of C_A/C_B. If $S_A > S_B$, the surface is enriched in B atoms, which now begin to sputter in greater profusion; i.e.,

$$\frac{\psi'_A}{\psi'_B} = \frac{S_A C'_A}{S_B C'_B} = \frac{S_A C_A}{S_B C_B}\frac{(1 - n_g S_A/n)}{(1 - n_g S_B/n)}. \tag{3-33}$$

Progressive change in the target surface composition alters the sputtered flux ratio to the point where it is equal to C_A/C_B, which is the same as the original target composition. Simultaneously, the target surface reaches the value $C'_A/C'_B = C_A S_B/C_B S_A$, which is maintained thereafter. A steady-state transfer of atoms from the bulk target to the plasma ensues, resulting in stoichiometric film deposition. This state of affairs persists until the target is consumed. Conditioning of the target by sputtering a few hundred layers is required to reach steady-state conditions. As an explicit example, consider the deposition of Permalloy films having atomic ratio 80 Ni–20 Fe from a target of this same composition. For 1-keV Ar, the sputter yields are $S_{Ni} = 2.2$ and

$S_{Fe} = 1.3$. The target surface composition is altered in the steady state to $C'_{Ni}/C'_{Fe} = 80(1.3)/20(2.2) = 2.36$, which is equivalent to 70.2 Ni and 29.8 Fe.

3.6.4. Thermal History of the Substrate (Ref. 21)

One of the important issues related to sputtering is the temperature rise in the substrate during film deposition. Sputtered atoms that impinge on the substrate are far more energetic than similar atoms emanating from an evaporation source. During condensation, this energy must be dissipated by the substrate, or else it may heat excessively, to the detriment of the quality of the deposited film. To address the question of substrate heating, we start with an equation describing the heat power balance, namely,

$$\rho c d(dT/dt) = P - L. \tag{3-34}$$

The term on the left is the net thermal energy per unit area per unit time (in typical units of watts/cm^2) retained by a substrate whose density, heat capacity, effective thickness, and rate of temperature rise are given by ρ, c, d, and dT/dt, respectively.

The incident power flux P has three important components:

1. Heat of condensation of atoms, ΔH_c (eV/atom).
2. Average kinetic energy of incident adatoms, $\bar{E}_k$ (eV/atom).
3. Plasma heating from bombarding neutrals and electrons. The plasma energy is assumed to be E_p (eV/atom).

Table 3-5 contains values for these three energies during magnetron sputtering at 1 keV (Ref. 22). For a deposition rate $\dot{d}$ (Å/min),

$$P = \frac{2.67 \times 10^{-29} \dot{d}(\Delta H_c + \bar{E}_k + E_p)}{\Omega} \text{ watts/cm}^2, \tag{3-35}$$

where Ω is the condensate atomic volume in cm^3/atom. The L term represents the heat loss to the substrate holder by conduction or to cooler surfaces in the chamber by radiation. For the moment, let us neglect L and calculate the temperature rise of a thermally isolated substrate. Substituting Eq. 3-35 into Eq. 3-34 and integrating, we obtain

$$T(t) = \frac{2.67 \times 10^{-29} \dot{d}(\Delta H_c + \bar{E}_k + E_p)t}{\rho c d \Omega}. \tag{3-36}$$

Consider Al deposited at a rate of 10,000 Å/min on a Si wafer 0.050 cm thick. For Al, $\Delta H_c + \bar{E}_k + E_p = 13$ eV/atom and $\Omega = 16 \times 10^{-24}$

Table 3-5. Energies Associated with Magnetron Sputtering

Metal	Heat of Condensation (eV/atom)	Kinetic Energy of Sputtered Atoms (eV/atom)	Plasma (eV/atom)	Estimated Flux (eV/atom)	Measured Flux (eV/atom)
Al	3.33	6	4	13	13
Ti	4.86	8	9	22	20
V	5.29	7	8	20	19
Cr	4.11	8	4	16	20
Fe	2.26	9	4	15	21
Ni	4.45	11	4	19	15
Cu	3.50	6	2	12	17
Zr	6.34	13	7	26	41
Nb	6.50	13	8	28	28
Mo	6.88	13	6	26	47
Rh	5.60	13	4	23	43
Cd	1.16	4	1	6	8
In	2.52	4	2	9	20
Hf	6.33	20	7	33	63
Ta	8.10	21	9	38	68
W	8.80	22	9	40	73
Au	3.92	13	2	19	23

From Ref. 22.

cm^3/atom, and for Si, $\rho = 2.3$ g/cm^3 and $c = 0.7$ J/g-°C. In depositing a film 1 μm thick, $t = 60$ sec, and the temperature rise of the substrate is calculated to be 162 °C. Higher deposition rates and substrates of smaller thermal mass will result in proportionately higher temperatures.

The temperature will not reach values predicted by Eq. 3-36 because of L. For simplicity we only consider heat loss by radiation. If the front and rear substrate surfaces radiate to identical temperature sinks at T_0 with equal emissivity ε, then $L = 2\sigma\varepsilon(T^4 - T_0^4)$, where σ, the Stefan–Boltzmann constant, equals 5.67×10^{-12} W/cm^2-K^4. Substitution in Eq. 3-34 and direct integration, after separation of variables, yields

$$t = \frac{1}{2\alpha^{3/2}\beta^{1/2}}\left[\tan^{-1}\sqrt{\frac{\beta}{\alpha}}\,T - \tan^{-1}\sqrt{\frac{\beta}{\alpha}}\,T_0 + \frac{1}{2}\ln\left(\frac{\sqrt{\alpha} + \sqrt{\beta}\,T}{\sqrt{\alpha} + \sqrt{\beta}\,T_0}\cdot\frac{\sqrt{\alpha} - \sqrt{\beta}\,T_0}{\sqrt{\alpha} - \sqrt{\beta}\,T}\right)\right], \tag{3-37}$$

where $\alpha = \sqrt{(2\sigma\varepsilon T_0^4 + P)/\rho cd}$ and $\beta = \sqrt{2\sigma\varepsilon/\rho cd}$.

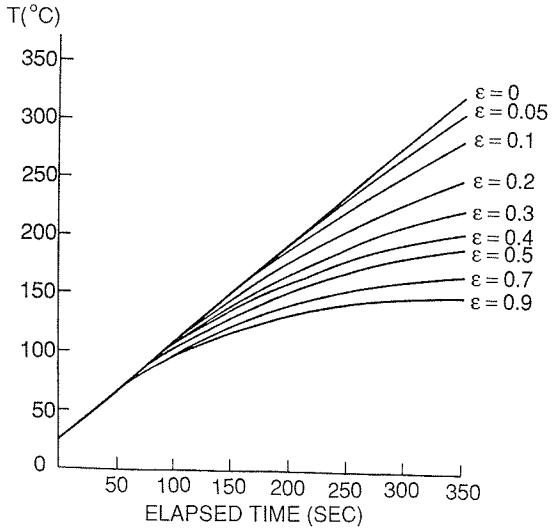

Figure 3-17. Temperature–time response for film–substrate combination under the influence of a power flux of 250 mW/cm^2. Deposition rate $\sim$ 1 μm/min. (Reprinted with permission from Cowan Publishing Co., from L. T. Lamont, *Solid State Technology* **22(9)**, 107, 1979).

Equation 3-37 expresses the time it takes for a substrate to reach temperature T starting from T_0, assuming radiation cooling. For short times Eq. 3-36 holds, whereas for longer times the temperature equilibrates to a radiation-limited value dependent on the incident power flux and substrate emissivity. Sputter deposition for most materials at the relatively high rate of 1 μm/min generates a typical substrate power flux of $\sim$ 250 mW/cm^2. The predicted rate of film heating is shown in Fig. 3-17. If substrate bias (Section 3.7.5.) is also applied, temperature increases can be quite substantial. In Al films, temperatures in excess of 200 °C have been measured. This partially accounts for enhanced atom mobility and step coverage during application of substrate bias.

Finally, we briefly consider sputter etching, a process that occurs at the target during sputtering. Films utilized in microelectronic applications must be etched in order to remove material and expose patterned regions for subsequent film deposition or doping processes. In the VLSI regime etching is carried out in plasmas and reactive gas environments, where the films involved essentially behave like sputtering targets. At the same power level, sputter etching rates tend to be lower, by more than an order of magnitude, than film deposition rates. This means that etching requires high power levels that frequently range from 1 to 2 W/cm^2. The combination of high power levels and long etching

times cause substrates to reach high radiation-limited temperatures. In Al, for example, temperature increases well in excess of 300 °C have been measured during etching.

3.7. Sputtering Processes

For convenience we divide sputtering processes into four cateogories: (1) dc, (2) RF, (3) magnetron, (4) reactive. We recognize, however, that there are important variants within each category (e.g., dc bias) and even hybrids between categories (e.g., reactive RF). Targets of virtually all important materials are commercially available for use in these sputtering processes. A selected number of target compositions representing the important classes of solids, together with typical sputtering applications for each are listed in Table 3-6.

In general, the metal and alloy targets are fabricated by melting either in vacuum or under protective atmospheres, followed by thermomechanical processing. Refractory alloy targets (e.g., Ti–W) are hot-pressed via the powder metallurgy route. Similarly, nonmetallic targets are generally prepared by hot-pressing of powders. The elemental and metal targets tend to have purities of 99.99% or better, whereas those of the nonmetals are generally less pure, with a typical upper purity limit of 99.9%. In addition, less than theoretical densities are achieved during powder processing. These metallurgical realities are sometimes reflected in emission of particulates, release of trapped gases, nonuniform target erosion, and deposited films of inferior quality. Targets are available in a variety of shapes (e.g., disks, toroids, plates, etc.) and sizes. Prior to use, they must be bonded to a cooled backing plate to avoid thermal cracking. Metal-filled epoxy cements of high thermal conductivity are employed for this purpose.

3.7.1. DC Sputtering

Virtually everything mentioned in the chapter so far has dealt with dc sputtering, also known as diode or cathodic sputtering. There is no need to further discuss the system configuration (Fig. 3-13), the discharge environment (Section 3.5), the ion–surface interactions (Section 3.6.1), or intrinsic sputter yields (Section 3.6.2). It is worthwhile, however, to note how the relative film deposition rate depends on the sputtering pressure and current variables. At low pressures, the cathode sheath is wide and ions are produced far from the target; their chances of being lost to the walls are great. The mean-free

Table 3-6. Sputtering Targets

Material	Application
1. *Metals*	
Aluminum	Metalization for integrated circuits, front surface mirrors
Chromium	Adhesion layers, resistor films (with SiO lithography master blanks
Germanium	Infrared filters
Gold	Contacts, reflecting films
Iron, nickel	Ferromagnetic films
Palladium, platinum	Contacts
Silver	Reflective films, contacts
Tantalum	Thin-film capacitors
Tungsten	Contacts
2. *Alloys*	
Al–Cu, Al–Si, Al–Cu–Si	Metalization for integrated circuits
Co–Fe, Co–Ni, Fe–Tb, Fe–Ni, Co–Ni–Cr	Ferromagnetic films
Ni–Cr	Resistors
Ti–W	Diffusion barriers in integrated circuits
Gd–Co	Magnetic bubble memory devices
3. *Oxides*	
Al_2O_3	Insulation, protective films for mirrors
$BaTiO_3$, $PbTiO_3$	Thin-film capacitors
CeO_2	Antireflection coatings
In_2O_3–SnO_2	Transparent conductors
$LiNbO_3$	Piezoelectric films
SiO_2	Insulation
SiO	Protective films for mirrors, infrared filters
Ta_2O_5, TiO_2, ZrO_2, HfO_2, MgO	Dielectric films for multilayer optical coatings
Yttrium aluminum oxide (YAG), yttrium iron oxide (YIG), $Gd_3Ga_5O_{12}$	Magnetic bubble memory devices
YVO_3–Eu_2O_3	Phosphorescent coating on special currency papers
$Cu_3Ba_2YO_7$	High temperature superconductors
4. *Fluorides*	
CaF_2, CeF_3, MgF_2, ThF_4, Na_3AlF_6 (cryolite)	Dielectric films for multilayer optical coatings (antireflection coatings, filters, etc.)
5. *Borides*	
TiB_2, ZrB_2	Hard, wear-resistant coatings
LaB_6	Thermionic emitters
6. *Carbides*	
SiC	High-temperature semiconduction
TiC, TaC, WC	Hard, wear-resistant coatings

Table 3-6. *Continued.*

Material	Application
7. *Nitrides*	
Si_3N_4	Insulation, diffusion barriers
TaN	Thin-film resistors
TiN	Hard coatings
8. *Silicides*	
$MoSi_2$, $TaSi_2$, $TiSi_2$, WSi_2	Contacts, diffusion barriers in integrated circuits
9. *Sulfides*	
CdS	Photoconductive films
MoS_2, TaS_2	Lubricant films for bearings and moving parts
ZnS	Multilayer optical coatings
10. *Selenides, tellurides*	
CdSe, PbSe, CdTe	Photoconductive films
ZnSe, PbTe	Optical coatings
MoTe, MoSe	Lubricants

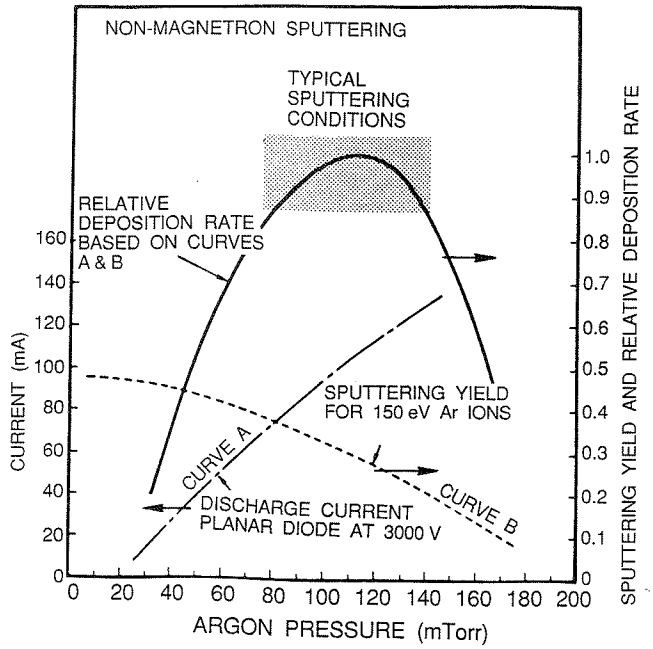

Figure 3-18. Influence of working pressure and current on deposition rate for nonmagnetron sputtering. (From Ref. 23).

electron path between collisions is large, and electrons collected by the anode are not replenished by ion-impact-induced cathode secondary emission. Therefore, ionization efficiencies are low, and self-sustained discharges cannot be maintained below about 10 mtorr. As the pressure is increased at a fixed voltage, the electron mean-free path is decreased, more ions are generated, and larger currents flow. But if the pressure is too high, the sputtered atoms undergo increased collisional scattering and are not efficiently deposited. The trade-offs in these opposing trends are shown in Fig. 3-18, and optimum operating conditions are shaded in. In general, the deposition rate is proportional to the power consumed, or to the square of the current density, and inversely dependent on the electrode spacing.

3.7.2. RF Sputtering

RF sputtering was invented as a means of depositing insulating thin films. Suppose we wish to produce thin SiO_2 films and attempt to use a quartz disk 0.1 cm thick as the target in a conventional dc sputtering system. For quartz $\rho \approx 10^{16}$ Ω-cm. To draw a current density J of 1 mA/cm^2, the cathode needs a voltage $V = 0.1\rho J$. Substitution gives an impossibly high value of 10^{12} V, which indicates why dc sputtering will not work. If we set a convenient level of $V = 100$ V, it means that a target with a resistivity exceeding 10^6 Ω-cm could not be dc-sputtered.

Now consider what happens when an ac signal is applied to the electrodes. Below about 50 kHz, ions are sufficiently mobile to establish a complete discharge at each electrode on each half-cycle. Direct current sputtering conditions essentially prevail at both electrodes, which alternately behave as cathodes and anodes. Above 50 kHz two important effects occur. Electrons oscillating in the glow region acquire enough energy to cause ionizing collisions, reducing the need for secondary electrons to sustain the discharge. Secondly, RF voltages can be coupled through any kind of impedance so that the electrodes need not be conductors. This makes it possible to sputter any material irrespective of its resistivity. Typical RF frequencies employed range from 5 to 30 MHz. However, 13.56 MHz has been reserved for plasma processing by the Federal Communications Commission and is widely used.

RF sputtering essentially works because the target *self*-biases to a negative potential. Once this happens, it behaves like a dc target where positive ion bombardment sputters away atoms for subsequent deposition. Negative target bias is a consequence of the fact that electrons are considerably more mobile than ions and have little difficulty in following the periodic change in the electric field. In Fig. 3-13b we depict an RF sputtering system schematically,

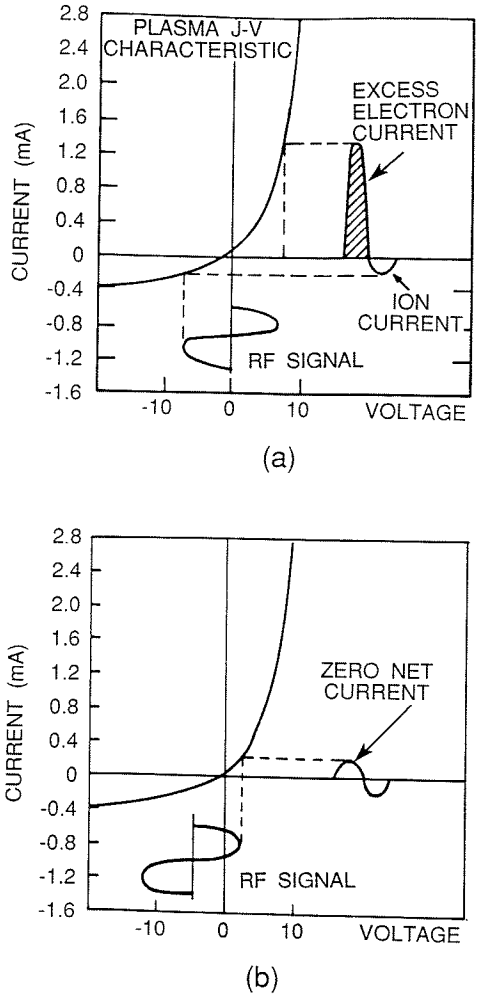

Figure 3-19. Formation of pulsating negative sheath on capacitively coupled cathode of RF discharge (a) Net current/zero self-bias voltage. (b) Zero current/nonzero self-bias voltage. (From Ref. 4).

where the target is capacitively coupled to the RF generator. The disparity in electron and ion mobilities means that isolated positively charged electrodes draw more electron current than comparably isolated negatively charged electrodes draw positive ion current. For this reason the discharge current–voltage characteristics are asymmetric and resemble those of a leaky rectifier or diode. This is indicated in Fig. 3-19, and even though it applies to a dc discharge, it helps to explain the concept of self-bias at RF electrodes.

As the pulsating RF signal is applied to the target, a large initial electron

current is drawn during the positive half of the cycle. However, only a small ion current flows during the second half of the cycle. This would enable a *net* current averaged over a complete cycle to be different from zero; but this cannot happen because no charge can be transferred through the capacitor. Therefore, the operating point on the characteristic shifts to a negative voltage —the target bias—and no *net* current flows.

The astute reader will realize that since ac electricity is involved, both electrodes should sputter. This presents a potential problem because the resultant film may be contaminated as a consequence. For sputtering from only one electrode, the sputter target must be an insulator and be capacitively coupled to the RF generator. The equivalent circuit of the sputtering system can be thought of as two series capacitors—one at the target sheath region, the other at the substrate—with the applied voltage divided between them. Since capacitive reactance is inversely proportional to the capacitance or area, more voltage will be dropped across the capacitor of a smaller surface area. Therefore, for efficient sputtering the area of the target electrode should be small compared with the total area of the other, or *directly* coupled, electrode. In practice, this electrode consists of the substrate stage and system ground, but it also includes baseplates, chamber walls, etc. It has been shown that the ratio of the voltage across the sheath at the (small) capacitively coupled electrode (V_c) to that across the (large) directly coupled electrode V_d is given by (Ref. 24)

$$V_c / V_d = (A_d / A_c)^4, \tag{3-38}$$

where A_c and A_d are the respective electrode areas. In essence, a steady-state voltage distribution prevails across the system similar to that shown in Fig. 3-15. The fourth-power dependence means that a large value of A_d is very effective in raising the target sheath potential while minimizing ion bombardment of grounded fixtures.

3.7.3. Magnetron Sputtering

3.7.3.1. *Electron Motion in Parallel Electric and Magnetic Fields.* Let us now examine what happens when a magnetic field of strength **B** is superimposed on the electric field $\mathscr{E}$ between the target and substrate. Such a situation arises in magnetron sputtering as well as in certain plasma etching configurations. Electrons within the dual field environment experience the well-known Lorentz force in addition to electric field force, i.e.,

$$\mathbf{F} = \frac{m\,dv}{dt} = -q(\mathscr{E} + \mathbf{v} \times \mathbf{B}), \tag{3-39}$$

where q, m and v are the electron charge, mass, and velocity, respectively.

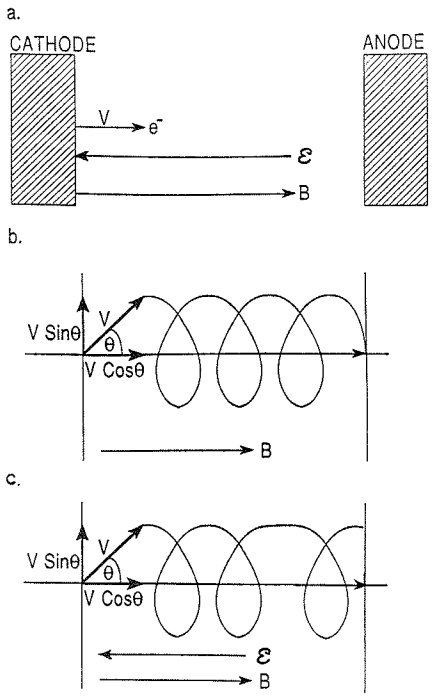

Figure 3-20. Effect of $\mathscr{E}$ and **B** on electron motion. (a) Linear electron trajectory when $\mathscr{E} \parallel \mathbf{B}$ ($\theta = 0$); (b) helical orbit of constant pitch when $\mathbf{B} \neq 0$, $\mathscr{E} = 0$, ($\theta \neq 0$); (c) helical orbit of variable pitch when $\mathscr{E} \parallel \mathbf{B}$ ($\theta \neq 0$).

First consider the case where **B** and $\mathscr{E}$ are parallel as shown in Fig. 3-20a. When electrons are emitted exactly normal to the target surface and parallel to both fields, then $\mathbf{v} \times \mathbf{B}$ vanishes; electrons are only influenced by the $\mathscr{E}$ field, which accelerates them toward the anode. Next consider the case where the $\mathscr{E}$ field is neglected but **B** is still applied as shown in Fig. 3-20b. If an electron is launched from the cathode with velocity v at angle θ with respect to **B**, it experiences a force $qvB \sin\theta$ in a direction perpendicular to **B**. The electron now orbits in a circular motion with a radius r that is determined by a balance of the centrifugal $(m(v \sin\theta)^2/r)$ and Lorentz forces involved, i.e., $r = mv \sin\theta / qB$. The electron motion is helical; in corkscrew fashion it spirals down the axis of the discharge with constant velocity $v \cos\theta$. If the magnetic field were not present, such off-axis electrons would tend to migrate out of the discharge and be lost at the walls.

The case where electrons are launched at an angle to parallel, uniform $\mathscr{E}$ and **B** fields is somewhat more complex. Corkscrew motion with constant radius occurs, but because of electron acceleration in the $\mathscr{E}$ field, the pitch of the helix lengthens with time (Fig. 3-20c). Time varying $\mathscr{E}$ fields complicate matters further and electron spirals of variable radius can occur. Clearly,

magnetic fields prolong the electron residence time in the plasma and thus enhance the probability of ion collisions. This leads to larger discharge currents and increased sputter deposition rates. Comparable discharges in a simple diode-sputtering configuration operate at higher currents and pressures. Therefore, applied magnetic fields have the desirable effect of reducing electron bombardment of substrates and extending the operating vacuum range.

3.7.3.2. Perpendicular Electric and Magnetic Fields. In magnetrons, electrons ideally do not even reach the anode but are trapped near the target, enhancing the ionizing efficiency there. This is accomplished by employing a magnetic field oriented parallel to the target and perpendicular to the electric field, as shown schematically in Fig. 3-21. Practically, this is achieved by placing bar or horseshoe magnets behind the target. Therefore, the magnetic field lines first emanate normal to the target, then bend with a component *parallel* to the target surface (this is the magnetron component) and finally return, completing the magnetic circuit. Electrons emitted from the cathode are initially accelerated toward the anode, executing a helical motion in the process; but when they encounter the region of the parallel magnetic field, they are bent in an orbit back to the target in very much the same way that electrons are deflected toward the hearth in an e-gun evaporator. By solving the coupled differential equations resulting from the three components of Eq. 3-39, we readily see that the parameric equations of motion are

$$y = \frac{q\mathscr{E}}{m\omega_c^2}(1 - \cos \omega_c t), \tag{3-40a}$$

$$x = \frac{\mathscr{E} t}{B}\left(1 - \frac{\sin \omega_c t}{\omega_c t}\right), \tag{3-40b}$$

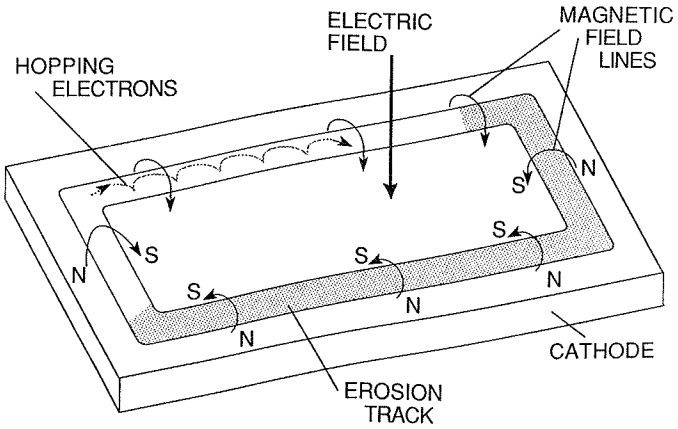

Figure 3-21. Applied fields and electron motion in the planar magnetron.

where y and x are the distances above and along the target, and $\omega_c = qB/m$. These equations describe a cycloidal motion that the electrons execute within the cathode dark space where both fields are present. If, however, electrons stray into the negative glow region where the $\mathscr{E}$ field is small, the electrons describe a circular motion before collisions may drive them back into the dark space or forward toward the anode. By suitable orientation of target magnets, a "race track" can be defined where the electrons hop around at high speed. Target erosion by sputtering occurs within this track because ionization of the working gas is most intense above it.

Magnetron sputtering is presently the most widely commercially practiced sputtering method. The chief reason for its success is the high deposition rates achieved (e.g., up to 1 μm/min for A1). These are typically an order of magnitude higher than rates attained by conventional sputtering techniques. Popular sputtering configurations utilize planar, toroidal (rectangular cross section), and toroidal–conical (trapezoidal cross section) targets (i.e., the S-gun). In commercial planar magnetron sputtering systems, the substrate plane translates past the parallel facing target through interlocked vacuum chambers to allow for semicontinuous coating operations. The circular (toridal–conical) target, on the other hand, is positioned centrally within the chamber, creating a deposition geometry approximating that of the analogous planar (ring) evaporation source. In this manner wafers on a planetary substrate holder can be coated as uniformly as with e-gun sources.923.7.4. Reactive Sputtering

In reactive sputtering, thin films of compounds are deposited on substrates by sputtering from metallic targets in the presence of a reactive gas, usually mixed with the inert working gas (invariably Ar). The most common compounds reactively sputtered (and the reactive gases employed) are briefly listed:

1. Oxides (oxygen)—Al_2O_3, In_2O_3, SnO_2, SiO_2, Ta_2O_5
2. Nitrides (nitrogen, ammonia)—TaN, TiN, AlN, Si_3N_4
3. Carbides (methane, acetylene, propane)—TiC, WC, SiC
4. Sulfides (H_2S)—CdS, CuS, ZnS
5. Oxycarbides and oxynitrides of Ti, Ta, Al, and Si

Irrespective of which of these materials is considered, during reactive sputtering the resulting film is either a solid solution alloy of the target metal doped with the reactive element (e.g., $TaN_{0.01}$), a compound (e.g., TiN), or some mixture of the two. Westwood (Ref. 25) has provided a useful way to visualize the conditions required to yield alloys or compounds. These two regimes are distinguished in Fig. 3-22a, illustrating the generic hysteresis curve for the total system pressure (P) as a function of the flow rate of

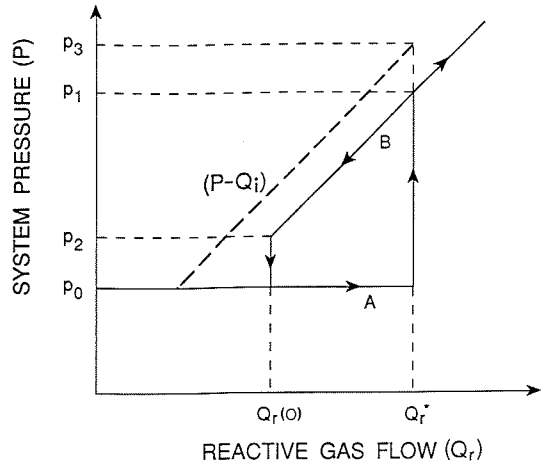

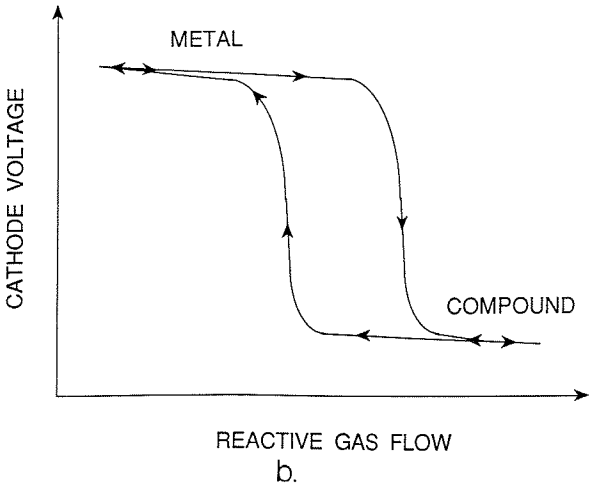

Figure 3-22. (a) Generic hysteresis curve for system pressure vs. reactive gas flow rate during reactive sputtering. Dotted line represents behavior with inert gas. (From Ref. 25). (b) Hysteresis curve of cathode voltage vs. reactive gas flow rate at constant discharge current.

reactive gas (Q_r) into the system. First, however, consider the dotted line representing the variation of P with flow rate of an *inert* sputtering gas (Q_i). Clearly, as Q_i increases, P increases because of the constant pumping speed (see Eq. 2-16). An example of this characteristic occurs during Ar gas sputtering of Ta. Now consider what happens when reactive N_2 gas is introduced into the system. As Q_r increases from $Q_r(0)$, the system pressure essentially remains at the initial value P_0 because N_2 reacts with Ta and is

removed from the gas phase. But beyond a critical flow rate Q_r^*, the system pressure jumps to the new value P_1. If no reactive sputtering took place, P would be somewhat higher (i.e., P_3). Once the equilibrium value of P is established, subsequent changes in Q_r cause P to increase or decrease linearly as shown. As Q_r decreases sufficiently, P again reaches the initial pressure.

The hysteresis behavior represents two stable states of the system with a rapid transition between them. In state A there is little change in pressure, while for state B the pressure varies linearly with Q_r. Clearly, all of the reactive gas is incorporated into the deposited film in state A—the doped metal and the atomic ratio of reactive gas dopant to sputtered metal increases with Q_r. The transition from state A to state B is triggered by compound formation on the metal target. Since ion-induced secondary electron emission is usually much higher for compounds than for metals, Ohm's law suggests that the *plasma* impedance is effectively lower in state B than in state A. This effect is reflected in the hysteresis of the target voltage with reactive gas flow rate, as schematically depicted in Fig. 3-22b.

The choice of whether to employ compound targets and sputter directly or sputter reactively is not always clear. If reactive sputtering is selected, then there is the option of using simple dc diode, RF, or magnetron configurations. Many considerations go into making these choices, and we will address some of them in turn.

3.7.4.1. Target Purity. It is easier to manufacture high-purity metal targets than to make high-purity compound targets. Since hot pressed and sintered compound powders cannot be consolidated to theoretical bulk densities, incorporation of gases, porosity, and impurities is unavoidable. Film purity using elemental targets is high, particularly since high-purity reactive gases are commercially available.

3.7.4.2. Deposition Rates. Sputter rates of metals drop dramatically when compounds form on the targets. Decreases in deposition rate well in excess of 50% occur because of the lower sputter yield of compounds relative to metals. The effect is very much dependent on reactive gas pressure. In dc discharges, sputtering is effectively halted at very high gas pressures, but the limits are also influenced by the applied power. Conditioning of the target in pure Ar is required to restore the pure metal surface and desired deposition rates. Where high deposition rates are a necessity, the reactive sputtering mode of choice is either dc or RF magnetron.

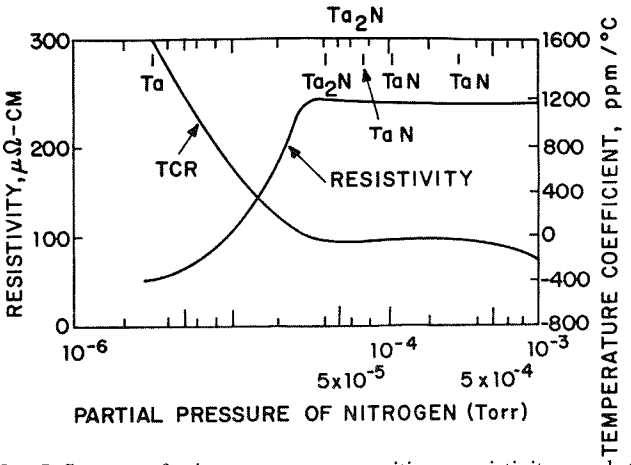

Figure 3-23. Influence of nitrogen on composition, resistivity, and temperature coefficient of resistivity of Ta films. (From Ref. 26).

3.7.4.3. Stoichiometry and Properties. Considerable variation in the composition and properties of reactively sputtered films is possible, depending on operating conditions. The case of tantalum nitride is worth considering in this regard. One of the first electronic applications of reactive sputtering involved deposition of TaN resistors employing dc diode sputtering at voltages of 3–5 kV, and pressures of about 30×10^{-3} torr. The dependence of the resistivity of "tantalum nitride" films is shown in Fig. 3-23, where either Ta, Ta_2N, TaN, or combinations of these form as a function of N_2 partial pressure. Color changes accompany the varied film stoichiometries. For example, in the case of titanium nitride films, the metallic color of Ti gives way to a light gold, then a rose, and finally a brown color with increasing nitrogen partial pressure.

3.7.5. Bias Sputtering

In bias sputtering, electric fields near the substrate are modified in order to vary the flux and energy of incident charged species. This is achieved by applying either a negative dc or RF bias to the substrate. With target voltages of -1000 to -3000 V, bias voltages of -50 to -300 V are typically used. Due to charge exchange processes in the anode dark space, very few discharge ions strike the substrate with full bias voltage. Rather a broad low energy distribution of ions and neutrals bombard the growing film. The technique has been utilized in all sputtering configurations (dc, RF, magnetron, and reactive).

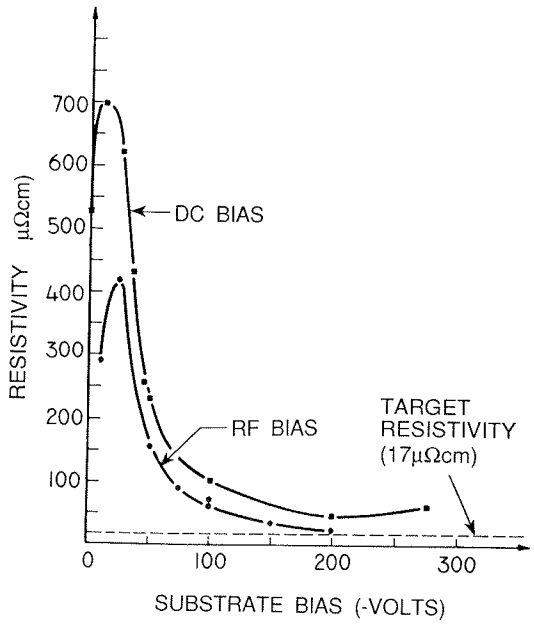

Figure 3-24. Resistivity of Ta films vs. substrate bias voltage; dc bias (3000 Å thick). (From Ref. 27). RF bias (1600 Å thick). (From Ref. 28).

Bias sputtering has been effective in altering a broad range of properties in deposited films. As specific examples we cite (Refs. 4–6).

a. *Resistivity*—A significant reduction in resistivity has been observed in metal films such as Ta, W, Ni, Au, and Cr. The similar variation in Ta film resistivity with dc or RF bias shown in Fig. 3-24 suggests that a common mechanism, independent of sputtering mode, is operative.
b. *Hardness and Residual Stress*—The hardness of sputtered Cr has been shown to increase (or decrease) with magnitude of negative bias voltage applied. Residual stress is similarly affected by bias sputtering.
c. *Dielectric Properties*—Increasing RF bias during RF sputtering of SiO_2 films has resulted in decreases in relative dielectric constant, but increases in resistivity.
d. *Etch Rate*—The wet chemical etch rate of reactively sputtered silicon nitride films is reduced with increasing negative bias.
e. *Optical Reflectivity*—Unbiased films of W, Ni, and Fe appear dark gray or black, whereas bias-sputtered films display metallic luster.
f. *Step Coverage*—Substantial improvement in step coverage of Al accompanies application of dc substrate bias.

g. *Film morphology*—The columnar microstructure of RF-sputtered Cr is totally disrupted by ion bombardment and replaced instead by a compacted, fine-grained structure (Ref. 18).
h. *Density*—Increased film density has been observed in bias-sputtered Cr (Ref. 18). Lower pinhole porosity and corrosion resistance are manifestations of the enhanced density.
i. *Adhesion*—Film adhesion is normally improved with ion bombardment of substrates during initial stages of film formation.

Although the details are not always clearly understood, there is little doubt that bias controls the film gas content. For example, chamber gases (e.g., Ar, O_2, N_2, etc.) sorbed on the growing film surface may be resputtered during low-energy ion bombardment. In such cases both weakly bound physisorbed gases (e.g., Ar) or strongly attached chemisorbed species (e.g., O or N on Ta) apparently have large sputtering yields and low sputter threshold voltages. In other cases, sorbed gases may have anomalously low sputter yields and will be incorporated within the growing film. In addition, energetic particle bombardment prior to and during film formation and growth promotes numerous changes and processes at a microscopic level, including removal of contaminants, alteration of surface chemistry, enhancement of nucleation and renucleation (due to generation of nucleation sites via defects, implanted, and recoil-implanted species), higher surface mobility of adatoms, and elevated film temperatures with attendant acceleration of atomic reaction and interdiffusion rates. Film properties are then modified through roughening of the surface, elimination of interfacial voids and subsurface porosity, creation of a finer, more isotropic grain morphology, and elimination of columnar grains—in a way that strongly dramatizes structure–property relationships in practice.

There are few ways to broadly influence such a wide variety of thin-film properties, in so simple and cheap a manner, than by application of substrate bias.

3.7.6. Evaporation versus Sputtering

Now that the details of evaporation and sputtering have been presented, we compare their characteristics with respect to process variables and resulting film properties. Distinctions in the stages of vapor species production, transport through the gas phase, and condensation on substrate surfaces for the two PVD processes are reviewed in tabular form in Table 3-7.

Table 3-7. Evaporation versus Sputtering

Evaporation	Sputtering
A. Production of Vapor Species	
1. Thermal evaporation mechanism	1. Ion bombardment and collisional momentum transfer
2. Low kinetic energy of evaporant atoms (at 1200 K, $E = 0.1$ eV)	2. High kinetic energy of sputtered atoms ($E = 2$–30 eV)
3. Evaporation rate (Eq. 3-2) (for $M = 50$, $T = 1500$ K, and $P_e = 10^{-3}$) $\approx 1.3 \times 10^{17}$ atoms/cm^2-sec.	3. Sputter rate (at 1 mA/cm^2 and $S = 2$) $\approx 3 \times 10^{16}$ atoms/cm^2-sec
4. Directional evaporation according to cosine law	4. Directional sputtering according to cosine law at high sputter rates
5. Fractionation of multicomponent alloys, decomposition, and dissociation of compounds	5. Generally good maintenance of target stoichiometry, but some dissociation of compounds.
6. Availability of high evaporation source purities	6. Sputter targets of all materials are available; purity varies with material
B. The Gas Phase	
1. Evaporant atoms travel in high or ultrahigh vacuum ($\sim 10^{-6}$–10^{-10} torr) ambient	1. Sputtered atoms encounter high-pressure discharge region ($\sim$ 100 mtorr)
2. Thermal velocity of evaporant 10^5 cm/sec	2. Neutral atom velocity $\sim 5 \times 10^4$ cm/sec
3. Mean-free path is larger than evaporant–substrate spacing. Evaporant atoms undergo no collisions in vacuum	3. Mean-free path is less than target–substrate spacing. Sputtered atoms undergo many collisions in the discharge
C. The Condensed Film	
1. Condensing atoms have relatively low energy	1. Condensing atoms have high energy
2. Low gas incorporation	2. Some gas incorporation
3. Grain size generally larger than for sputtered film	3. Good adhesion to substrate
4. Few grain orientations (textured films)	4. Many grain orientations

3.8. Hybrid and Modified PVD Processes

This chapter concludes with a discussion of several PVD processes that are more complex than the conventional ones considered up to this point. They demonstrate the diversity of process hybridization and modification possible in

producing films with unusual properties. Ion plating, reactive evaporation, and ion-beam-assisted deposition will be the processes considered first. In the first two, the material deposited usually originates from a heated evaporation source. In the third, well-characterized ion beams bombard films deposited by evaporation or sputtering. The chapter closes with a discussion of ionized cluster-beam deposition. This process is different from others considered in this chapter in that film formation occurs through impingement of collective groups of atoms from the gas phase rather than individual atoms.

3.8.1. Ion Plating

Ion plating, developed by Mattox (Ref. 29), refers to evaporated film deposition processes in which the substrate is exposed to a flux of high-energy ions capable of causing appreciable sputtering before and during film formation. A schematic representation of a diode-type batch, ion-plating system is shown in Fig. 3-25a. Since it is a hybrid system, provision must be made to sustain the plasma, cause sputtering, and heat the vapor source. Prior to deposition, the substrate, negatively biased from 2 to 5 kV, is subjected to inert-gas ion bombardment at a pressure in the millitorr range for a time sufficient to sputter-clean the surface and remove contaminants. Source evaporation is then begun without interrupting the sputtering, whose rate must obviously be less than that of the deposition rate. Once the interface between film and substrate has formed, ion bombardment may or may not be continued. To circumvent the relatively high system pressures associated with glow discharges, high-vacuum ion-plating systems have also been constructed. They rely on directed ion beams targeted at the substrate. Such systems, which have been limited thus far to research applications, are discussed in Section 3.8.3.

Perhaps the chief advantage of ion plating is the ability to promote extremely good adhesion between the film and substrate by the ion and particle bombardment mechanisms discussed in Section 3.7.5. A second important advantage is the high "throwing power" when compared with vacuum evaporation. This results from gas scattering, entrainment, and sputtering of the film, and enables deposition in recesses and on areas remote from the source–substrate line of sight. Relatively uniform coating of substrates with complex shapes is thus achieved. Lastly, the quality of deposited films is frequently enhanced. The continual bombardment of the growing film by high-energy ions or neutral atoms and molecules serves to peen and compact it to near bulk densities. Sputtering of loosely adhering film material, increased surface diffusion, and reduced shadowing effects serve to suppress undesirable columnar growth.

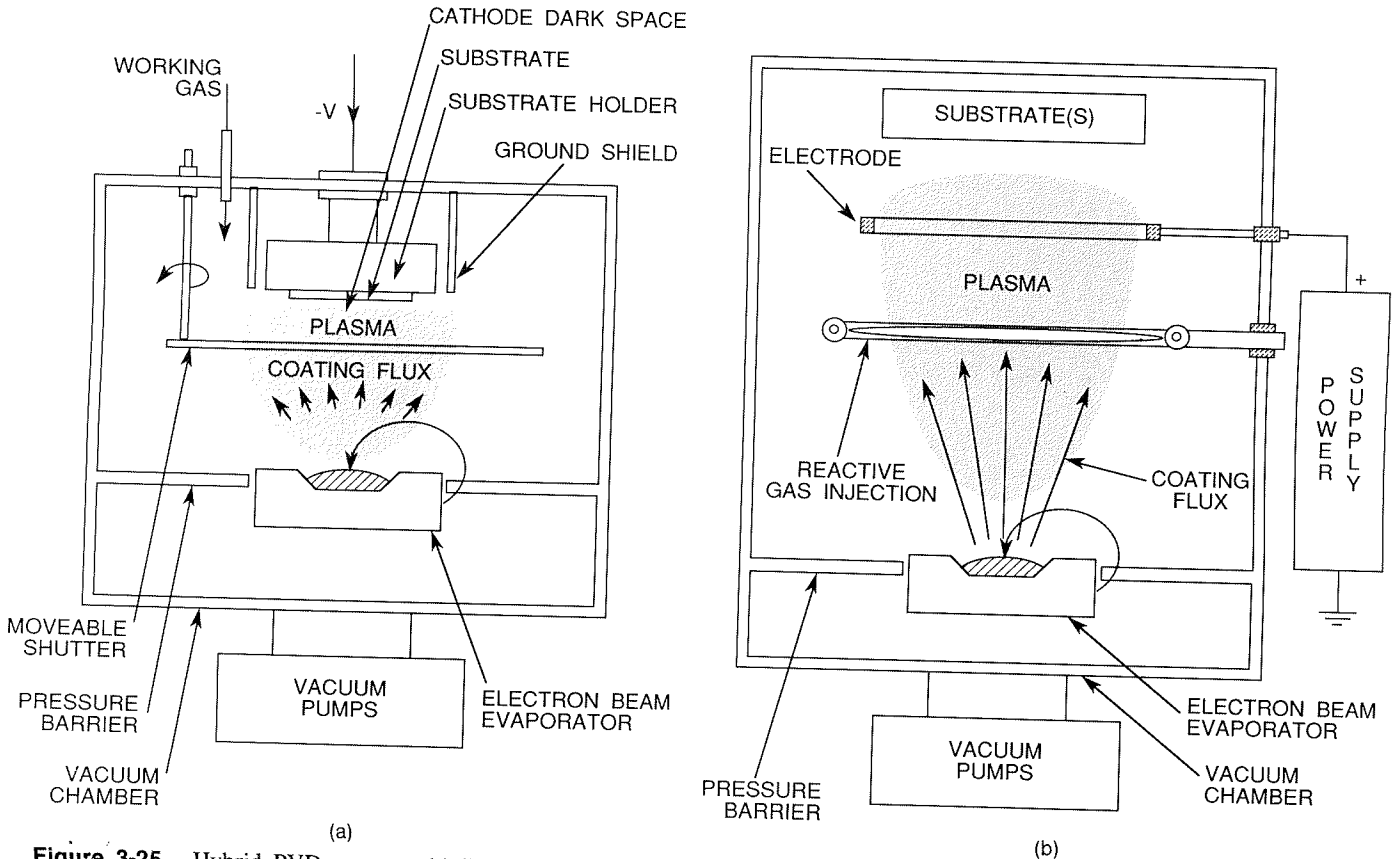

Figure 3-25. Hybrid PVD process: (a) Ion plating. (From Ref. 29). (b) Activated reactive evaporation. (From Ref. 30). (c) Ion-beam-assisted deposition. (From Ref. 31).

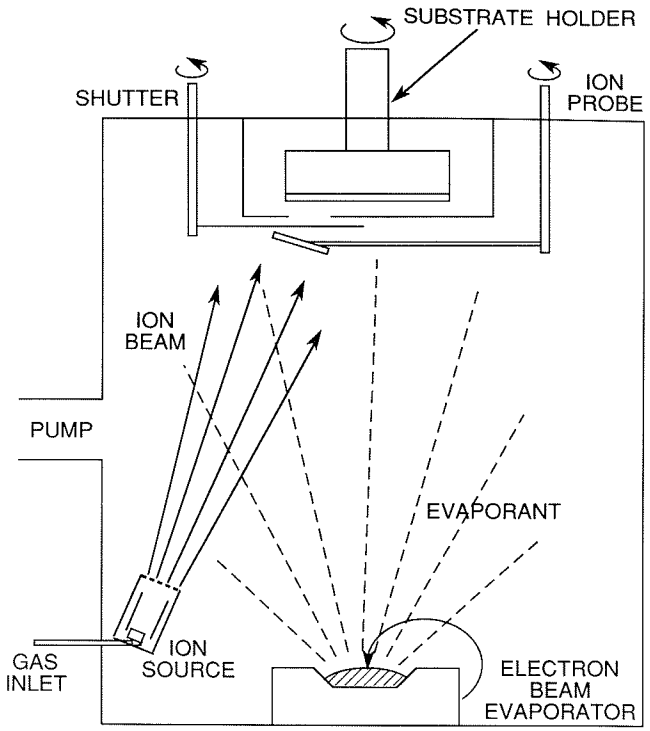

Figure 3-25. *Continued.*

A major use of ion plating has been to coat steel and other metals with very hard films for use in tools and wear-resistant applications. For this purpose, metals like Ti, Zr, Cr, and Si are electron-beam-evaporated through an Ar plasma in the presence of reactive gases such as N_2, O_2, and CH_4, which are simultaneously introduced into the system. This variant of the process is known as reactive ion plating (RIP), and coatings of nitrides, oxides, and carbides have been deposited in this manner.

3.8.2. Reactive Evaporation Processes

In reactive evaporation the evaporant metal vapor flux passes through and reacts with a gas (at $1-30 \times 10^{-3}$ torr) introduced into the system to produce compound deposits. The process has a history of evolution in which evaporation was first carried out without ionization of the reactive gas. In the more recent activated evaporation (ARE) processes developed by Bunshah and

Figure 3-25. Hybrid PVD process: (a) Ion plating. (From Ref. 29). (b) Activated reactive evaporation. (From Ref. 30). (c) Ion-beam-assisted deposition. (From Ref. 31).

co-workers (Ref. 30), a plasma discharge is maintained directly within the reaction zone between the metal source and substrate. Both the metal vapor and reactive gases, such as O_2, N_2, CH_4, C_2H_2, etc., are, therefore, ionized increasing their reactivity on the surface of the growing film or coating, promoting stoichiometric compound formation. One of the process configurations is illustrated in Fig. 3-25b, where the metal is melted by an electron beam. A thin plasma sheath develops on top of the molten pool. Low-energy secondary electrons from this source are drawn upward into the reaction zone by a circular wire electrode placed above the melt biased to a positive dc potential (20–100 V), creating a plasma-filled region extending from the electron-beam gun to near the substrate. The ARE process is endowed with considerable flexibility, since the substrates can be grounded, allowed to float electrically, or biased positively or negatively. In the latter variant ARE is quite similar to RIP. Other modifications of ARE include resistance-heated evaporant sources coupled with a low-voltage cathode (electron) emitter–anode assembly. Activation by dc and RF excitation has also been employed to sustain the plasma, and transverse magnetic fields have been applied to effectively extend plasma electron lifetimes.

Before considering the variety of compounds produced by ARE, we recall that thermodynamic and kinetic factors are involved in their formation. The high negative enthalpies of compound formation of oxides, nitrides, carbides, and borides indicate no thermodynamic obstacles to chemical reaction. The rate-controlling step in simple reactive evaporation is frequently the speed of the chemical reaction at the reaction interface. The actual physical location of the latter may be the substrate surface, the gas phase, the surface of the metal evaporant pool, or a combination of these. Plasma activation generally lowers the energy barrier for reaction by creating many excited chemical species. By eliminating the major impediment to reaction, ARE processes are thus capable of deposition rates of a few thousand angstroms per minute.

A partial list of compounds synthesized by ARE methods includes the oxides αAl_2O_3, V_2O_3, TiO_2, indium–tin oxide; the carbides TiC, ZrC, NbC, Ta_2C, W_2C, VC, HfC; and the nitrides TiN, MoN, HfN, and cubic boron nitride. The extremely hard TiN, TiC, Al_2O_3, and HfN compounds have found extensive use as coatings for sintered carbide cutting tools, high-speed drills, and gear cutters. As a result, they considerably increase wear resistance and extend tool life. In these applications ARE processing competes with the CVD methods discussed in Chapters 4 and 12. The fact that no volatile metal-bearing compound is required as in CVD is an attractive advantage of ARE. Most significantly, these complex compound films are synthesized at relatively low temperatures; this is a unique feature of plasma-assisted deposition processes.

3.8.3. Ion-Beam-Assisted Deposition Processes (Ref. 31)

We noted in Section 3.7.5 that ion bombardment of biased substrates during sputtering is a particularly effective way to modify film properties. Process control in plasmas is somewhat haphazard, however, because the direction, energy, and flux of the ions incident on the growing film cannot be regulated. Ion-beam-assisted processes were invented to provide independent control of the deposition parameters and, particularly, the characteristics of the ions bombarding the substrate. Two main ion source configurations are employed. In the dual-ion-beam system, one source provides the inert or reactive ion beam to *sputter* a target in order to yield a flux of atoms for deposition onto the substrate. Simultaneously, the second ion source, aimed at the substrate, supplies the inert or reactive ion beam that bombards the depositing film. Separate film-thickness-rate and ion-current monitors, fixed to the substrate holder, enable the two incident beam fluxes to be independently controlled.

In the second configuration (Fig. 3-25c), an ion source is used in conjunction with an *evaporation* source. The process, known as ion-assisted deposition (IAD), combines the benefits of high film deposition rate and ion bombardment. The energy flux and direction of the ion beam can be regulated independently of the evaporation flux. In both configurations the ion-beam angle of incidence is not normal to the substrate and can lead to anisotropic film properties. Substrate rotation is, therefore, recommended if isotropy is desired.

Broad-beam (Kaufman) ion sources, the heart of ion-beam-assisted deposition systems, were first used as ion thrusters for space propulsion (Ref. 32). Their efficiency has been optimized to yield high-ion-beam fluxes for given power inputs and gas flows. They contain a discharge chamber that is raised to a potential corresponding to the desired ion energy. Gases fed into the chamber become ionized in the plasma, and a beam of ions is extracted and accelerated through matching apertures in a pair of grids. Current densities of several mA/cm^2 are achieved. (Note that 1 mA/cm^2 is equivalent to 6.25×10^{15} $ions/cm^2$-sec or several monolayers per second.) The resulting beams have a low-energy spread (typically 10 eV) and are well collimated, with divergence angles of only a few degrees. Furthermore, the background pressure is quite low ($\sim 10^{-4}$ torr) compared with typical sputtering or etching plasmas.

Examples of thin-film property modification as a result of IAD are given in Table 3-8. The reader should appreciate the applicability to all classes of solids and to a broad spectrum of properties. For the most part, ion energies are lower than those typically involved in sputtering. Bombarding ion fluxes are generally smaller than depositing atom fluxes. Perhaps the most promising

Table 3-8. Property Modification by Ion Bombardment during Film Deposition

Film material	Ion species	Property modified	Ion energy (eV)	Ion/Atom Arrival Rate Ratio
Ge	Ar^+	Stress, adhesion	65–3000	2×10^{-4} to 10^{-1}
Nb	Ar^+	Stress	100–400	3×10^{-2}
Cr	Ar^+, Xe^+	Stress	3,400–11,500	8×10^{-3} to 4×10^{-2}
Cr	Ar^+	Stress	200–800	$\sim 7 \times 10^{-3}$ to 2×10^{-2}
SiO_2	Ar^+	Step coverage	500	0.3
SiO_2	Ar^+	Step coverge	~ 1–80	~ 4.0
AlN	N_2^+	Preferred orientation	300–500	0.96 to 1.5
Au	Ar^+	Coverage at 50 Å thickness	400	0.1
GdCoMo	Ar^+	Magnetic anisotropy	~ 1–150	~ 0.1
Cu	Cu^+	Improved epitaxy	50–400	10^{-2}
BN	$(B–N–H)^+$	Cubic structure	200–1000	~ 1.0
ZrO_2, SiO_2, TiO_2	Ar^+, O_2^+	Refractive index, amor → crys	600	2.5×10^{-2} to 10^{-1}
SiO_2, TiO_2	O_2^+	Refractive index	300	0.12
SiO_2, TiO_2	O_2^+	Optical transmission	30–500	0.05 to 0.25
Cu	N^+, Ar^+	Adhesion	50,000	10^{-2}
Ni on Fe	Ar^+	Hardness	10,000–20,000	~ 0.25

From Ref. 32.

application of ion bombardment is the enhancement of the density and index of refraction of optical coatings. This subject is treated again in Chapter 11.

3.8.4. Ionized Cluster Beam (ICB) Deposition (Ref. 33)

The idea of employing energetic ionized clusters of atoms to deposit thin films is due to T. Takagi. In this novel technique, vapor-phase aggregates or clusters, thought to contain a few hundred to a few thousand atoms, are

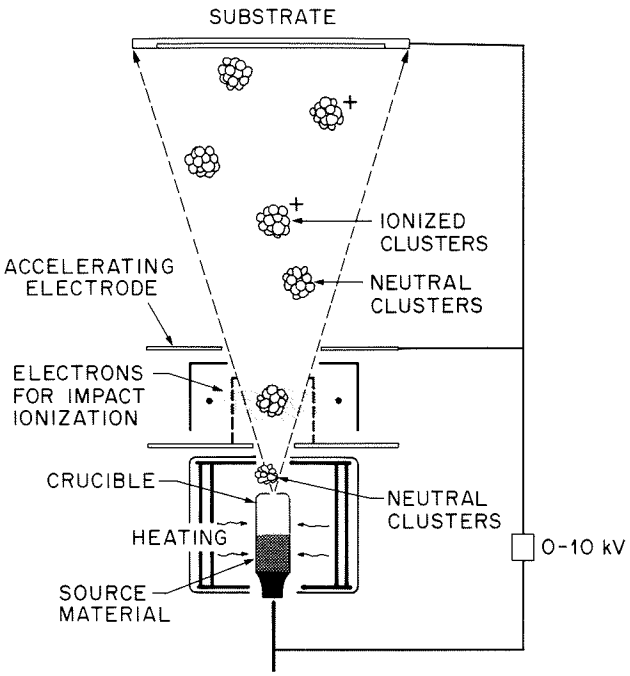

Figure 3-26. Schematic diagram of ICB system. (Courtesy of W. L. Brown, AT&T Bell Laboratories. Reprinted with permission of the publisher from Ref. 34).

created, ionized, and accelerated toward the substrate as depicted schematically in Fig. 3-26. As a result of impact with the substrate, the cluster breaks apart, releasing atoms to spread across the surface. Cluster production is, of course, the critical step and begins with evaporation from a crucible containing a small aperture or nozzle. The evaporant vapor pressure is much higher (10^{-2}–10 torr) than in conventional vacuum evaporation. For cluster formation the nozzle diameter must exceed the mean-free path of vapor atoms in the crucible. Viscous flow of atoms escaping the nozzle then results in an adiabatic supersonic expansion and the formation of stable cluster nuclei. Optimum expansion further requires that the ratio of the vapor pressure in the crucible to that in the vacuum chamber exceed 10^4 to 10^5.

The arrival of ionized clusters with the kinetic energy of the acceleration voltage (0–10 kV), and neutral clusters with the kinetic energy of the nozzle ejection velocity, affects film nucleation and growth processes in the following ways:

1. The local temperature at the point of impact increases.
2. Surface diffusion of atoms is enhanced.

3. Activated centers for nucleation are created.
4. Coalescence of nuclei is fostered.
5. At high enough energies, the surface is sputter-cleaned, and shallow implantation of ions may occur.
6. Chemical reactions between condensing atoms and the substrate or gas-phase atoms are favored.

Moreover, the magnitude of these effects can be modified by altering the extent of electron impact ionization and the accelerating voltage.

Virtually all classes of film materials have been deposited by ICB (and variant reactive process versions), including pure metals, alloys, intermetallic compounds, semiconductors, oxides, nitrides, carbides, halides, and organic compounds. Special attributes of ICB-prepared films worth noting are strong adhesion to the substrate, smooth surfaces, elimination of columnar growth morphology, low-temperature growth, controllable crystal structures, and, importantly, very high quality single-crystal growth (epitaxial films). Large Au film mirrors for CO_2 lasers, ohmic metal contacts to Si and GaP, electromigration- (Section 8.4) resistant Al films, and epitaxial Si, GaAs, GaP, and InSb films deposited at low temperatures are some examples indicative of the excellent properties of ICB films. Among the advantages of ICB deposition are vacuum cleanliness ($\sim 10^{-7}$ torr in the chamber) of evaporation and energetic ion bombardment of the substrate, two normally mutually exclusive features. In addition, the interaction of slowly moving clusters with the substrate is confined, limiting the amount of damage to both the growing film and substrate. Despite the attractive features of ICB, the formation of clusters and their role in film formation are not well understood. Recent research (Ref. 34), however, clearly indicates that the total number of atoms agglomerated in large metal clusters is actually very small (only 1 in 10^4) and that only a fraction of large clusters is ionized. The *total* energy brought to the film surface by ionized clusters is, therefore, quite small. Rather, it appears that individual atomic ions, which are present in much greater profusion than are ionized clusters, are the dominant vehicle for transporting energy and momentum to the growing film. In this respect, ICB deposition belongs to the class of processes deriving benefits from the ion-beam-assisted film growth mechanisms previously discussed.

EXERCISES

1. Employing Figs. 3-1 and 3-2, calculate values for the molar heat of vaporization of Sn and Ga.

2. Design a laboratory experiment to determine a working value of the heat of vaporization of a metal employing common thin-film deposition and characterization equipment.

3. Suppose Fe satisfactorily evaporates from a surface source, 1 cm^2 in area, which is maintained at 1550 °C. Higher desired evaporation rates are achieved by raising the temperature 100 °C. But doing this will burn out the source. Instead, the melt area is increased without raising its temperature. By what factor should the source area be enlarged?

4. A molecular-beam epitaxy system contains separate Al and As effusion evaporation sources of 4 cm^2 area, located 10 cm from a (100) GaAs substrate. The Al source is heated to 1000 °C, and the As source is heated to 300 °C. What is the growth rate of the AlAs film in Å/sec? [*Note:* AlAs basically has the same crystal structure and lattice parameter (5.661 Å) as GaAs.]

5. How far from the substrate, in illustrative problem on p. 90, would a *single* surface source have to be located to maintain the same deposited film thickness tolerance?

6. An Al film was deposited at a rate of 1 μm/min in vacuum at 25 °C, and it was estimated that the oxygen content of the film was 10^{-3}. What was the partial pressure of oxygen in the system?

7. Alloy films of Ti–W, used as diffusion barriers in integrated circuits, are usually sputtered. The Ti–W, phase diagram resembles that of Ge–Si (Fig. 1-13) at elevated temperatures.

   a. Comment on the ease or feasibility of evaporating a 15 wt% Ti–W alloy.
   b. During sputtering with 0.5-keV Ar, what composition will the target surface assume in the steady state?

8. In order to deposit films of the alloy YBa_2Cu_3, the metals Y, Ba, and Cu are evaporated from three *point* sources. The latter are situated at the corners of an equilateral triangle whose side is 20 cm. Directly above the centroid of the source array, and parallel to it, lies a small substrate; the deposition system geometry is thus a tetrahedron, each side being 20 cm long.

   a. If the Y source is heated to 1740 K to produce a vapor pressure of 10^{-3} torr, to what temperature must the Cu source be heated to maintain film stoichiometry?

b. Rather than a point source, a surface source is used to evaporate Cu. How must the Cu source temperature be changed to ensure deposit stoichiometry?
c. If the source configuration in part (a) is employed, what *minimum* O_2 partial pressure is required to deposit stoichiometric $YBa_2Cu_3O_7$ superconducting films by a reactive evaporation process? The atomic weights are Y = 89, Cu = 63.5, Ba = 137, and O = 16.

9. One way to deposit a thin metal film of known thickness is to heat an evaporation source to dryness (i.e., until no metal remains in the crucible). Suppose it is desired to deposit 5000 Å of Au on the internal spherical surface of a hemispherical shell measuring 30 cm in diameter.

a. Suggest two different evaporation source configurations (source type and placement) that would yield uniform coatings.
b. What weight of Au would be required for each configuration, assuming evaporation to dryness?

10. Suppose the processes of electron impact ionization and secondary emission of electrons by ions control the current J in a sputtering system according to the Townsend equation (Ref. 19)

$$J = \frac{J_0 \exp \alpha d}{1 - \gamma[\exp(\alpha d) - 1]},$$

where J_0 = primary electron current density from external source
α = number of ions per unit length produced by electrons
γ = number of secondary electrons emitted per incident ion
d = interelectrode spacing.

a. If the film deposition rate during sputtering is proportional to the product of J and S, calculate the proportionality constant for Cu in this system if the deposition rate is 200 Å/min for 0.5-keV Ar ions. Assume $\alpha = 0.1$ ion/cm, $\gamma = 0.08$ electron/ion, $d = 10$ cm, and $J_0 = 100$ mA/cm^2.
b. What deposition rate can be expected for 1-keV Ar if $\alpha = 0.5$ ion/cm and $\gamma = 0.1$ electron/ion.

11. In a dc planar magnetron system operating at 1000 V, the anode–cathode spacing is 10 cm. What magnetic field should be applied to trap electrons within 1 cm of the target?

12. At what sputter deposition rate of In on a Si substrate will the film melt within 1 min? The melting point of In is 155 °C.

13. a. During magnetron sputtering of Au at 1 keV, suppose there are two collisions with Ar atoms prior to deposition. What is the energy of the depositing Au atoms? (Assume Ar is stationary in a collision.)

b. The probability that gas-phase atoms will travel a distance x *without* collision is $\exp - x/\lambda$, where λ is the mean-free path between collisions. Assume λ for Au in Ar is 5 cm at a pressure of 1 mtorr. If the target–anode spacing is 12 cm, at what operating pressure will 99% of the sputtered Au atoms undergo gas-phase collisions prior to deposition?

14. For a new application it is desired to continuously coat a 1-m-wide steel strip with a 2-μm-thick coating of Al. The x-y dimensions of the steel are such that an array of electron-beam gun evaporators lies along the y direction and maintains a uniform coating thickness across the strip width. How fast should the steel be fed in the x direction past the surface sources, which can evaporate 20 g of Al per second? Assume that Eq. 3-18 holds for the coating thickness along the x direction, that the source–strip distance is 30 cm, and that the steel sheet is essentially a horizontal substrate 40 cm long on either side of the source before it is coiled.

15. Select the appropriate film deposition process (evaporation, sputtering, etc., sources, targets, etc.) for the following applications:

a. Coating a large telescope mirror with Rh
b. Web coating of potato chip bags with Al films
c. Deposition of Al–Cu–Si thin-film interconnections for integrated circuits
d. Deposition of TiO_2–SiO_2 multilayers on artificial gems to enhance color and reflectivity

16. Theory indicates that the kinetic energy (E) and angular spread of neutral atoms sputtered from a surface are given by the distribution function

$$F(E,\theta) = CS\frac{E}{(E+U)^3}\cos\theta,$$

where U = binding energy of surface atoms
C = constant
θ = angle between sputtered atoms and the surface normal.

a. Sketch the dependence of $f(E,\theta)$ vs. E for two values of U.
b. Show that the maximum in the energy distribution occurs at $E = U/2$.

17. a. To better visualize the nucleation of clusters in the ICB process, schematically indicate the free energy of cluster formation vs. cluster size as a function of vapor supersaturation (see Section 1.7).

b. What vapor supersaturation is required to create a 1000-atom cluster of Au if the surface tension is 1000 ergs/cm^2?

c. If such a cluster is ionized and accelerated to an energy of 10 keV, how much energy is imparted to the substrate by each cluster atom?

REFERENCES

1. W. R. Grove, *Phil. Trans. Roy. Soc., London A* **142**, 87 (1852).
2. M. Faraday, *Phil. Trans.* **147**, 145 (1857).
3.* R. Glang, in *Handbook of Thin Film Technology*, eds. L. I. Maissel and R. Glang, McGraw-Hill, New York (1970).
4.* J. L. Vossen and J. J. Cuomo, in *Thin Film Processes*, eds. J. L. Vossen and W. Kern, Academic Press, New York (1978).
5.* W. D. Westwood, in *Microelectronic Materials and Processes*, ed. R. A. Levy, Kluwer Academic, Dordrecht (1989).
6.* B. N. Chapman, *Glow Discharge Processes*, Wiley, New York (1980).
7. C. H. P. Lupis, *Chemical Thermodynamics of Materials*, North-Holland, Amsterdam (1983).
8. R. E. Honig, *RCA Rev.* **23**, 567 (1962).
9.* H. K. Pulker, *Coatings on Glass*, Elsevier, New York, (1984).
10. Examples taken from *Physical Vapor Deposition*, Airco-Temescal (1976).
11. L. Holland, *Vacuum Deposition of Thin Films*, Wiley, New York (1956).
12. C. H. Ting and A. R. Neureuther, *Solid State Technol.* **25(2)**, 115 (1982).
13. H. L. Caswell, in *Physics of Thin Films*, Vol. 1, ed. G. Hass, Academic Press, New York (1963).
14. L. D. Hartsough and D. R. Denison, *Solid State Technology* **22(12)**, 66 (1979).
15. *Handbook—The Optical Industry and Systems Directory*, H-11 (1979).
16. E. B. Grapper, *J. Vac. Sci. Technol.* **5A(4)**, 2718 (1987); **8**, 333 (1971).

*Recommended texts or reviews.

17. P. Archibald and E. Parent, *Solid State Technol.* **19(7)**, 32 (1976).
18. D. M. Mattox, *J. Vac. Sci. Technol.* **A7(3)**, 1105 (1989).
19.* A. B. Glaser and G. E. Subak-Sharpe, *Integrated Circuit Engineering*, Addison-Wesley, Reading, MA (1979).
20. P. Sigmund, *Phys. Rev.* **184** 383 (1969).
21. L. T. Lamont, *Solid State Technol.* **22(9)**, 107 (1979).
22. J. A. Thornton, *Thin Solid Films* **54**, 23 (1978).
23. J. A. Thornton, in *Thin Film Processes*, eds. J. L. Vossen and W. Kern, Academic Press, New York (1978).
24. H. R. Koenig and L. I. Maissel, *IBM J. Res. Dev.* **14**, 168 (1970).
25.* W. D. Westwood, in *Physics of Thin Films*, Vol. 14, eds. M. H. Francombe and J. L. Vossen, Academic Press, New York (1989).
26.* L. I. Maissel and M. H. Francombe, *An Introduction to Thin Films*, Gordon and Breach, New York, (1973).
27. L. I. Maissel and P. M. Schaible, *J. Appl. Phys.* **36**, 237 (1965).
28. J. L. Vossen and J. J. O'Neill, *RCA Rev.* **29**, 566 (1968).
29. D. M. Mattox, *J. Vac. Sci. Technol.* **10**, 47 (1973).
30.* R. F. Bunshah and C. Deshpandey, in *Physics of Thin Films*, Vol. 13, eds. M. H. Francombe and J. L. Vossen, Academic Press, New York (1987).
31. J. M. E. Harper and J. J. Cuomo, *J. Vac. Sci. Technol.* **21(3)** (1982).
32. J. M. E. Harper, J. J. Cuomo, R. J. Gambino, and H. R. Kaufman, in *Ion Beam Modification of Surfaces*, eds. O. Auciello and R. Kelly, Elsevier, Amsterdam (1984).
33.* T. Takagi, in *Physics of Thin Films*, Vol. 13, eds. M. H. Francombe and J. L. Vossen, Academic Press, New York (1987).
34. W. L. Brown, M. F. Jarrold, R. L. McEachern, M. Sosnowski, G. Takaoka, H. Usui and I. Yamada, *Nuclear Instruments and Methods in Physics Research*, to be published (1991).